Geochemistry, Geophysics, Geosystems®

RESEARCH ARTICLE
10.1029/2025GC012354

# Subduction Zone Magnetism: The Influence of Metamorphism and Serpentinization in the Mantle Wedge

**Y. Li[1,2], P. C. Lindquist[3], D. Han[1], B. Fish[1], R. J. Harrison[2], W. McCarthy[4], R. M. Palin[1], C. B. Condit[3], and C. I. O. Nichols[1]**

[1]Department of Earth Sciences, University of Oxford, Oxford, UK, [2]Department of Earth Sciences, University of Cambridge, Cambridge, UK, [3]Department of Earth and Space Sciences, University of Washington, Seattle, WA, USA, [4]School of Earth and Environmental Sciences, University of St. Andrews, St. Andrews, UK

**Abstract** Subduction zone magnetic anomalies have previously been used to infer their thermal structure assuming a uniformly serpentinized mantle carries a homogeneous, isotropic magnetization. However, seismic tomography, geological observations and numerical modeling provide increasing evidence for a non-uniformly serpentinized mantle wedge that may carry heterogeneous magnetization. In this study, we characterize the rock magnetic properties in variably serpentinized samples from Santa Catalina Island/Pimu'nga in California, USA, and uncover at least two populations of magnetite formed during metamorphism and serpentinization of the mantle wedge. All samples contain Cr-magnetite, which is believed to form through the amphibolite facies metamorphism of Cr-spinel under high fluid:rock ratios, as opposed to serpentinization reactions, which have been invoked for mantle wedge magnetism in the past. Heavily serpentinized samples contain stoichiometric magnetite associated with serpentinization reactions under wedge conditions. We propose that the observed magnetic anomalies above subduction zones are primarily controlled by two factors: (a) the extent of fluids available for metamorphism of the mantle wedge and the transformation of Cr-spinel to Cr-magnetite and (b) the extent of subsequent serpentinization which may generate a layer of heavily serpentinized rock containing a mixture of Cr- and stoichiometric magnetite at the base of the mantle wedge. This proposal precludes the direct connection between subduction zone magnetic anomalies and thermal structure without prior characterization of fluid availability for both metamorphism and serpentinization, and its implications on wedge magnetic mineralogy.

**Plain Language Summary** The mantle wedge is a triangular prism of rock that lies between an overlying tectonic plate and underlying subducting slab in a subduction zone. Rocks from the mantle wedge have been brought up from great depth and exposed on the surface of Santa Catalina Island/Pimu'nga, USA. Samples collected from the island provide a rare opportunity to directly study an ancient hydrated mantle wedge. We are particularly interested in the magnetic properties of these samples, which affect surface magnetic measurements. We find at least two compositionally distinct groups of magnetic minerals formed through different processes: (a) metamorphic change and (b) hydration reactions. The two magnetic types of magnetic mineral possess different magnetic properties, and so affect surface magnetic measurements in different ways. Surface magnetic measurements can be used to infer subduction zone thermal structure, which is greatly important for assessing their potential as seismic and volcanic hazards. As such, a better understanding of the magnetic properties of mantle rock can facilitate improvements in understanding the natural hazards associated with subduction zones.

**Key Points:**

- Variably serpentinized mantle wedge rocks proximal to an early Cretaceous paleosubduction interface are exposed on Santa Catalina Island
- Samples all contain Cr-magnetite, which is genetically unrelated to stoichiometric magnetite found only in heavily serpentinized samples
- Cr-magnetite has different magnetic properties to the stoichiometric magnetite that's typically used to interpret magnetic anomalies

**Supporting Information:**

Supporting Information may be found in the online version of this article.

**Correspondence to:**

Y. Li,
y.li@esc.cam.ac.uk

**Citation:**

Li, Y., Lindquist, P. C., Han, D., Fish, B., Harrison, R. J., McCarthy, W., et al. (2026). Subduction zone magnetism: The influence of metamorphism and serpentinization in the mantle wedge. *Geochemistry, Geophysics, Geosystems*, *27*, e2025GC012354. https://doi.org/10.1029/2025GC012354

Received 7 APR 2025
Accepted 19 FEB 2026



## 1. Introduction

Subduction zones host the Earth's largest and deepest earthquakes (Gardonio et al., 2024) and their associated tsunami hazard, with the three largest moment magnitude ($Mw > 8$) earthquakes since 2000 (Briggs et al., 2006; Hirose et al., 2011; Lay et al., 2005) occurring at subduction interfaces. Furthermore, over three-quarters of documented Holocene volcanic eruptions occur at convergent plate margins above subduction zones (Siebert et al., 2015). Seismicity and volcanism along subduction zones are both fundamentally controlled by thermal structure (van Keken & Wilson, 2023). The large-scale thermal structure of a subduction zone (which includes the subducted slab and mantle wedge) cannot be ascertained directly, and their structures are typically approximated using a geodynamic modeling approach based on heat flow measurements and guided by seismic and geodetic

observations. However, this modeling approach cannot uniquely define thermal structure and significant uncertainties remain (Syracuse et al., 2010; van Keken & Wilson, 2023).

Surface magnetic measurements have been used as an additional constraint on the thermal structure of continental regions in the past (Bhattacharyya & Leu, 1975; Blakely, 1988; Okubo et al., 1985; Tanaka et al., 1999), and more recently of subduction zones (Manea & Manea, 2011; Teknik et al., 2024). Magnetic minerals lose their magnetization above a mineral-specific temperature known as the Curie temperature, which is 580 °C at 0.7 GPa (~23 km, which roughly corresponds to depths at which the Curie temperature is reached) (Schult, 1970) for pure magnetite—a common magnetic mineral in Earth's mantle (Ferré et al., 2020). The Curie temperature is lower for titanomagnetite, $Fe_{3-x}Ti_xO_4$ (on the order of 370–430 °C for $x = 0.33$ and 160–180 °C for $x = 0.57$; Bowles et al. (2019)), one of the most significant magnetic minerals in the crust (Blakely, 1988; Dunlop & Özdemir, 2015) and Cr-magnetite, $Fe^{2+}(Fe_{1-n}Cr_n)_2O_4$ (~530 °C for $n = 0.1$ and ~500 °C for $n = 0.2$; Hodel et al. (2020)), which can form in the mantle through the metamorphic alteration of Cr-spinels (Farahat, 2008; Hodel et al., 2020). The depth below which rocks lose their magnetization, known as the Curie point depth (CPD), can be solved for using magnetic anomaly maps under the assumption that all lithospheric magnetization is induced and isotropic. CPDs can therefore be used to produce a depth map of an isothermal surface, potentially providing a powerful constraint for lithospheric thermal models. On the global scale over continents or oceans, the assumption of induced and isotropic magnetization is supported by comparisons of data against models of the latitudinal dependence of magnetic intensity under the assumption of induced versus remanent magnetization (Maus & Haak, 2002). When regional-scale CPDs are computed over subduction zones, significant discrepancies between the magnetically- and geodynamically derived 580 °C isotherm are found (Manea & Manea, 2011), suggesting that the predicted isotherm is inaccurate, non-stoichiometric magnetite is present and/or that the assumption of isotropic, induced magnetization may not hold where oceanic lithosphere subducts beneath continental lithosphere.

Here, we analyze the rock magnetic properties of a collection of sheared, variably serpentinized mantle wedge serpentinites from Santa Catalina Island/Pimu'nga, California, USA (Figure 1a). We focus on rock magnetic properties for magnetite grain populations formed under the pressure and temperature conditions associated with regional metamorphism and serpentinization in the mantle wedge. After identifying each population of magnetic grains, we then relate the effect of metamorphism and variable serpentinization to rock magnetic properties. By matching these magnetic properties to geologically, seismically and numerically constrained mantle wedge serpentinization maps from Reynard (2013), Xia et al. (2015) and Lee and Kim (2021)—where a broad zone of partial serpentinization overlies a layer of heavy serpentinization and shearing above the subduction interface (Figure 1f), as well as qualitative mantle wedge pressure-temperature ($P$-$T$) maps that reflect variable metamorphism in the wedge, we construct a tentative conceptual model for subduction zone magnetic structure.

## 2. Background

### 2.1. Magnetite Formation in Subduction Zone Settings and the Interpretation of Curie Point Depths

A diverse range of magnetite compositions can be found in and around subduction zones depending on their mechanism of formation. Stoichiometric magnetite can form through the oxidation of Fe atoms freed from mantle silicates (e.g., olivine and pyroxene) during serpentinization (Saad, 1969). Cr-magnetite can form through the metamorphic (rather than serpentinization driven) change of primary/mantle Cr-spinels, particularly under high fluid:rock conditions and greenschist to amphibolite metamorphic facies environments (Farahat, 2008). Lower fluid:rock ratios are less conducive to the metamorphism of Cr-spinel to Cr-magnetite, allowing persistence of more extensive Cr-spinel cores (Farahat, 2008), which may be modified by later processes. Ti-magnetite tends to be less common or more Ti-poor in subduction zone environments (relative to mid-ocean ridge environments), which is attributed to the suppression of Ti incorporation into the magnetite structure during growth by oxidizing subduction-derived fluids (Xu et al., 2025).

Previous studies have focused on (titano)magnetite grains as found in the lithosphere, which are typically taken to be coarse-grained (Thébault, 2021)—that is, multidomain—such that their Curie and blocking temperatures are equivalent. As a result, the depth of lithospheric demagnetization is taken to be the CPD. The CPD is found by inverting crustal magnetic anomaly maps using spectral methods (Bouligand et al., 2009; Ravat et al., 2007; Tanaka et al., 1999). Though depth itself can affect the Curie temperature (via pressure effects), typical variations in CPD ($<\pm$10 km, corresponding to $<\pm\sim$ 0.3 GPa or 3 kbar) give rise to negligible variations in magnetite Curie

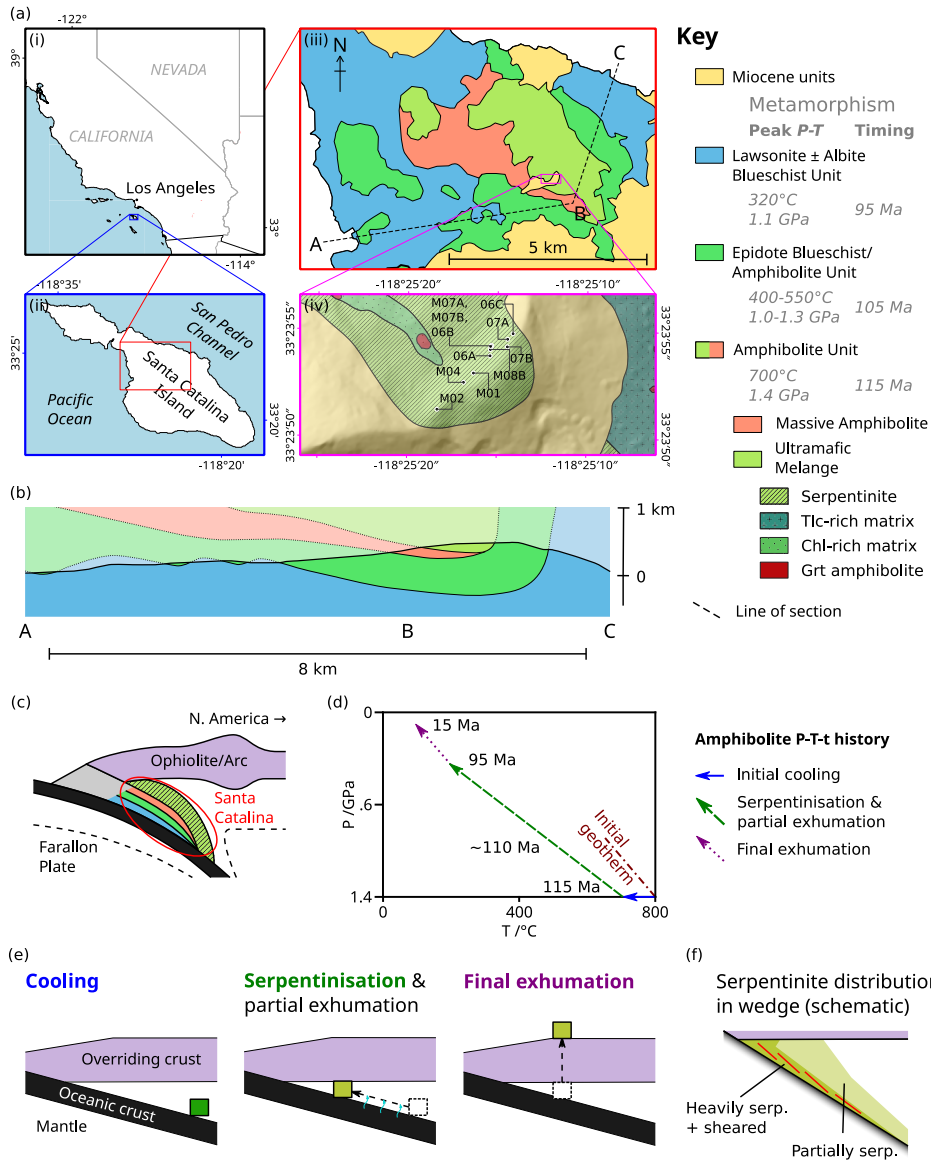


**Figure 1.** (a) Location (i,ii) and geological (iii,iv) maps showing the geographic and geological context of the sampling site in the Ultramafic Mélange Unit, which is part of the Santa Catalina Amphibolite Unit. (a-iii) is after Platt (1975); Platt and Schmidt (2024), (a-iv) contains geology after Platt et al. (2020) and topography after Tyler and Danielson (2018) (b) Geological cross-section taken across the line on (a-iii) showing the relation between the four main units, after Platt and Schmidt (2024). (c) Tectonic interpretation of the Santa Catalina Subduction Complex before surface exhumation after Figure 10d of Grove and Bebout (1995). (d) A simplified *P-T-t* path of the Santa Catalina Amphibolite Unit. (e) Schematic geological history corresponding to the *P-T-t* path in (d) both of which are simplified after Grove and Bebout (1995); Grove et al. (2008); Platt and Schmidt (2024). (f) Schematic representation of the distribution of heavily serpentinized and sheared rock and partially serpentinized rock (Reynard, 2013; Xia et al., 2015). In key: peak *P-T* conditions after Figure 4 of Platt and Schmidt (2024), timing of metamorphism from Figure 10 of Grove et al. (2008).

temperature through pressure effects (<±5.55 °C, or < ± 1%, given the magnetite CPD/pressure gradient of 1.85 °C/kbar) (Schult, 1970; Table 1). Therefore, the resulting CPD maps are interpreted to represent an isothermal surface and have been used in previous studies as an additional constraint on lithospheric thermal structure. For example, Blakely (1988) applied this principle to the extensional Basin and Range Province within Nevada, finding a good match between regional differences in inferred CPD and direct heat flow measurements, linking regions of high heat flow and shallow CPD to thinned, extending lithosphere. These spectral methods treated rock magnetization as isotropic and roughly parallel to the ambient field (Blakely, 1988; Connard et al., 1983), and

**Table 1**
*Normalized X-Ray Fluorescence, Corrected Protolith (Initial Boundary Condition) and Corrected Final Serpentinite (End Boundary Condition) Compositions in wt% for the Five Analyzed Samples*

| Sample | SiO2 | TiO2 | Al2O3 | MnO | MgO | CaO | Na2O | K2O | P2O5 | $H_2O$ | FeO | Fe2O3 | O |
|---|---|---|---|---|---|---|---|---|---|---|---|---|---|
| Measured Data | | | | | | | | | | | | | |
| 23C-06B | 40.01 | 0.03 | 1.40 | 0.12 | 34.15 | 0.13 | 0.04 | 0.02 | 0.01 | 13.56 | 0.95 | 6.98 | |
| 23C-06C | 45.22 | 0.01 | 0.73 | 0.13 | 32.72 | 0.07 | 0.03 | 0.01 | 0.01 | 11.79 | 0.69 | 6.79 | |
| 23C-07A | 38.96 | 0.04 | 1.78 | 0.11 | 35.67 | 0.20 | 0.04 | 0.01 | 0.01 | 12.10 | 1.35 | 7.83 | |
| 23C-07B | 39.41 | 0.03 | 1.43 | 0.09 | 36.08 | 0.07 | 0.04 | 0.01 | 0.02 | 12.64 | 0.74 | 7.34 | |
| 23C-M02 | 39.92 | 0.01 | 1.46 | 0.09 | 35.18 | 0.05 | 0.08 | 0.01 | 0.02 | 12.87 | 0.73 | 7.38 | |
| Corrected Data for Protolith/Initial Composition | | | | | | | | | | | | | |
| 23C-06B | 36.87 | 0.03 | 0.90 | | 55.39 | 0.14 | 0.04 | 0.01 | | 0.01 | 6.57 | | 0.03 |
| 23C-06C | 36.64 | 0.01 | 0.49 | | 56.15 | 0.07 | 0.04 | 0.01 | | 0.01 | 6.55 | | 0.03 |
| 23C-07A | 37.12 | 0.03 | 1.07 | | 54.30 | 0.21 | 0.04 | 0.01 | | 0.01 | 7.17 | | 0.03 |
| 23C-07B | 36.78 | 0.02 | 0.88 | | 55.81 | 0.05 | 0.04 | 0.01 | | 0.01 | 6.37 | | 0.03 |
| 23C-M02 | 36.84 | 0.01 | 0.91 | | 55.55 | 0.03 | 0.08 | 0.01 | | 0.01 | 6.54 | | 0.03 |
| Corrected Data for Serpentinite/Final Composition | | | | | | | | | | | | | |
| 23C-06B | 26.13 | 0.02 | 0.54 | | 33.25 | 0.09 | 0.03 | 0.01 | | 35.20 | 3.95 | | 0.79 |
| 23C-06C | 30.83 | 0.00 | 0.29 | | 33.25 | 0.04 | 0.02 | 0.00 | | 30.90 | 3.88 | | 0.78 |
| 23C-07A | 26.23 | 0.02 | 0.71 | | 35.79 | 0.14 | 0.03 | 0.00 | | 31.41 | 4.73 | | 0.95 |
| 23C-07B | 26.15 | 0.01 | 0.56 | | 35.69 | 0.03 | 0.03 | 0.00 | | 32.64 | 4.07 | | 0.81 |
| 23C-M02 | 26.43 | 0.00 | 0.57 | | 34.72 | 0.02 | 0.05 | 0.00 | | 33.30 | 4.09 | | 0.82 |

*Note.* In the corrected compositions, Iron (III) oxide is replaced by excess oxygen that acts on Iron (II) oxide. For the pre-apatite compositions (i.e., just the water, silica and iron oxidation corrections), see Table S3 in Supporting Information S1. All rows are normalized.

tend to treat the Curie depth as corresponding to the magnetite Curie temperature isotherm at 580 °C for the purposes of interpretation, though with the caveat that the Curie temperature may vary based on variable magnetic mineralogy in the crust—for example, high Ti content in titanomagnetite may drastically reduce its Curie temperature (Blakely, 1988). While this assumption may be suitable for continental regions without extensive coeval metasomatism or metamorphic change such that magnetic mineralogy is unlikely to vary much laterally, subduction zones provide a much more chemically varied environment that give rise to systematically varying magnetic mineralogies.

Blakely et al. (2005) investigated magnetic anomalies across the Cascadian continental arc within Oregon and found the observed crustal magnetic anomalies over subduction zones include a contribution from the underlying mantle wedge. This observation was interpreted as wedge magnetization resulting from the generation of (stoichiometric) magnetite during wedge hydration and serpentinization. The magnetic anomalies overlying subduction zones were further studied by Manea and Manea (2011), who found that, unlike in continental regions, subduction zone CPDs above Mexico are significantly shallower than those predicted by geodynamical models of subduction zone thermal structure. By combining heat flow measurements with inferred CPD depths and comparing them to the regional tectonic structure, the discrepancies with the model-derived thermal structure were attributed to isotherm shallowing by arc magmatism. In the earlier study of Tanaka et al. (1999), the broad correspondence of high heat flow to shallowed CPD was also noted. However, this relation is absent in several locations within the study region, such as the volcanic front near Tohoku, Japan (very high surface heat flow without shallower CPD relative to the hinterland with lower heat flow; Figure 3a of Tanaka et al. (1999)) and the Okinawa Trough, South Japan (locally shallowed CPD at 125°E with no observed increase in surface heat flow; Figure 3c of Tanaka et al. (1999)).

Previous studies treat the magnetized mantle wedge as a single, uniformly magnetized block, ignoring the effect of variable regional metamorphism and local serpentinization (e.g., Blakely et al., 2005). However, Saad (1969)

analyzed variably serpentinized rocks from an ultramafic intrusion and predicted an increase in strength of induced magnetization with increasing serpentinization due to magnetite grain growth. Additionally, both geological and seismic evidence indicate heterogeneous serpentinization in subduction zones (Reynard, 2013; Xia et al., 2015), warranting further investigation into the effect of fluid–rock interactions on the resulting magnetic anomalies over subduction zones.

### 2.2. Geology of Santa Catalina Island/Pimu'nga

The Catalina Schist on Santa Catalina Island/Pimu'nga is an exhumed paleosubduction terrane (Grove & Bebout, 1995; Platt, 1975). Subduction along the western margin of North America during the Cretaceous resulted in the underplating of packages of metamafic and metasedimentary rocks from the downgoing oceanic crust that make up the majority of the Catalina Schist. These packages vary in peak metamorphic temperature and subduction age from the structurally highest and oldest Amphibolite Unit to the lowest and youngest Blueschist Unit, a sequence that is likely the result of progressive underplating and cooling (Figure 1) (Grove & Bebout, 1995; Grove et al., 2008; Harvey, Penniston-Dorland, et al., 2021; Platt, 1975; Platt & Schmidt, 2024). We focus on the Amphibolite Unit, which contains a large proportion of serpentinized peridotites that has been interpreted to represent an entrained portion of the over-riding mantle wedge during subduction (Figure 1c) (Platt, 1975; Sorensen, 1988).

The Amphibolite Unit is divided into a structurally lower coherent mafic gneiss topped by metasedimentary schist, overlain by a zone that consists of a massive serpentinite domain in the west (Platt, 1976; Platt & Schmidt, 2024), and an ultramafic mélange-dominated domain in the east close to Catalina Airport (Grove & Bebout, 1995; Sorensen, 1988). This amphibolite mélange contains garnet amphibolite, serpentinite, and rare metasedimentary blocks within a metasomatic matrix that developed via chemical and mechanical mixing of mafic and ultramafic rocks (Bebout & Barton, 2002).

Peak metamorphic temperatures of 650–730°C in the Amphibolite Unit were determined using Zr-in-rutile thermometry for mafic and metasedimentary blocks recovered from within the mélange (Harvey, Penniston-Dorland, et al., 2021; Penniston-Dorland et al., 2018). Original pressure estimates of 0.8–1.1 GPa for the Amphibolite Unit were based on mineral assemblages and pyroxene compositions from blocks and rinds (Sorensen & Barton, 1987), but more recent quartz-in-garnet barometry from blocks in the mélange suggest pressures of 1.34–1.44 GPa (Harvey, Penniston-Dorland, et al., 2021).

The samples presented here were collected from a∼ km-scale serpentinite block in the mélange-dominated domain of the Amphibolite Unit (Figure 1a). Petrological studies indicate that serpentinites formed from harzburgitic and dunitic protoliths within the mantle wedge hanging wall of the paleosubduction interface (Platt, 1975; Sorensen, 1988). Garnet geochronology suggests that metamorphism of coherent amphibolites and amphibolite mélange rocks occurred ∼116–108 Ma ago (Harvey, Walker, et al., 2021). Underplating of this unit occurred by 109–108 Ma ago recorded by $^{40}Ar/^{39}Ar$ hornblende ages in mélanges of the younger and lower epidote amphibolite unit indicating that the active plate interface localized to the epidote amphibolite unit by this time (Grove & Bebout, 1995; Grove et al., 2008). White mica $^{40}Ar/^{39}Ar$ ages in the Amphibolite Unit indicate that these rocks had cooled to 350–450°C by 105–100 Ma ago, and ages from the lowest-grade lawsonite-albite units suggest that all the units of the Catalina Schist had reached ∼200°C and ∼0.4 GPa by ∼95 Ma ago (Grove & Bebout, 1995). The units remained at these conditions until recent exhumation along a relatively linear *P-T*path to the surface during Miocene extension ∼15 Ma ago (Figure 1d).

Serpentinization of the original peridotites in the Amphibolite Unit is inferred to have occurred during partial exhumation following the development of peak temperature mineral assemblages in other Amphibolite Unit lithologies. This inferred petrogenesis is based on the dominance of the lower-temperature serpentine minerals lizardite and chrysotile, the preservation in serpentine textures of original olivine- and orthopyroxene-defined fabrics (Platt, 1975, 1976), and presence of serpentine veins that cross-cut orthopyroxene and chlorite pods (Sorensen, 1988).

## 3. Methods

We analyzed a total of 12 non-oriented, variably serpentinized samples (06A, 06B, 06C, 07A, 07B, M01(A), M02, M04, M07A1, M07A2, M07B, M08B), all of which had their average color and density determined from

hand sample. We also analyzed eight thin sections using micropetrographic methods, including two thin sections from sample M07B (06C, 07A, M04, M08B, M01A, M02, M07B1, M07B2).

Energy dispersive spectroscopy (EDS) maps were acquired from regions around veins in three samples (06C, M01A, M02), as well as for groundmass magnetite grains in three different samples (07A, M07B2, M08B); electron probe spot compositions were acquired for magnetite and serpentine, amphibole and clinochlore grains in four samples (06C, M01A, M04, M08B); magnetite grain orientations were acquired for one cluster in sample M07B1. Bulk compositions were determined for five hand samples (06B, 06C, 07A, 07B, M02). Magnetic hysteresis properties were measured for all hand samples except M07A2. Anisotropy of magnetic susceptibility (AMS) measurements were made on all hand samples except M07B. Temperature dependence of magnetic susceptibility measurements were made for M08B, 07B and M07A1.

### 3.1. Electron Microscopy

EDS maps for 06C, M01A and M02 were acquired using a Thermo Scientific Apreo-S Scanning Electron Microscope (SEM) with an Oxford Instruments Ultim Max EDS detector at the Molecular Analysis Facility at the University of Washington. Qualitative elemental abundance maps were collected using a 20 keV beam voltage and 0.8 nA beam current for at least the following elements: Al, Ca, Cr, Fe, K, Mg, Mn, Na, Ni, Si. Additional element maps collected for the different regions are specified by sample region in Table S1 in Supporting Information S1. EDS maps used to identify magnetite compositions were acquired for M01A, 06C, 07A, M07B2, and M08B using an FEI Quanta 650 SEM with an Oxford Instruments EDS detector at the Department of Earth Sciences, University of Oxford. Energy spectra were acquired at 20 keV accelerating voltage at Spot 5 for major and minor elements. EDS maps of major and minor elements were processed in AZtec, and raw maps were recompiled in TruMap mode to correct for background noise.

Major and minor element spot compositions of magnetite, amphibole, clinochlore and serpentine grains were acquired using a CAMECA SX-5 FE electron microprobe at the Department of Earth Sciences, University of Oxford, UK. A 15 keV beam voltage and 10 nA beam current were used for all silicate grains, and a 15 keV beam voltage and 20 nA beam current were used for all magnetite grains.

Magnetite grain orientations were found for one magnetite cluster in thin section sample M07B1 using a Zeiss EVO MA10 SEM equipped with a Bruker Quanta e-Flash 1000 EBSD detector at the David Cockayne Center for Electron Microscopy, Department of Materials, University of Oxford. A 20 keV beam voltage and 20 nA beam current were used. The sample was positioned at a working distance of 28.1 mm with 70° tilt angle.

### 3.2. Bulk Rock Geochemistry

Whole-rock major element (oxides of: Si, Ti, Al, Fe, Mn, Mg, Ca, Na, K, P) abundances were measured using a Malvern PANalytical Zetium X-ray Fluorescence (XRF) vacuum spectrometer at the Department of Earth and Environment, Franklin and Marshall College, and the amount of ferrous iron determined by titration following the methodologies of Waterton et al. (2020) and Mertzman (2000). Loss On Ignition (LOI) was assumed to represent water weight only.

### 3.3. Density and Color Analysis

Densities of cm-scale hand samples were determined using the volume-difference method. Masses were measured using a Mettler PJ360 DeltaRange® mass balance. Characteristic sample colors were determined by averaging photographs of cut sample faces taken under the constant lighting of a Microtec HM-3 microscope and with constant camera exposure and white balance. Characteristic colors were reported in the form of pixel-averaged value, where the "value" of each pixel is the average of [R,G,B] contributions to that pixel's color. A lower value indicates a darker color.

### 3.4. Phase Equilibrium Modeling

Phase equilibrium modeling (PEM) was performed using Theriak-Domino (de Capitani & Brown, 1987; de Capitani & Petrakakis, 2010) to predict stable phase assemblages of the five bulk-rock compositions along a pressure-temperature-composition (*P*-*T*-X) path simulating cooling of the ambient mantle by the new subducting slab (with the decrease in temperature resulting in metamorphic change under amphibolite facies condition),

serpentinization due to an influx of fluids during subduction, and subsequent late-stage exhumation (Figure 1d). Though the cooling and final exhumation stages are included for completeness (and to predict stable silicate/major mineral assemblages), the purpose of this modeling is primarily to characterize the formation of (stoichiometric) magnetite during the serpentinization stage. The rocks' geological history was modeled in the chemical system CaO–FeO–$O_2$–MgO–$Al_2O_3$–$SiO_2$–$TiO_2$–$Na_2O$-$K_2O$-$H_2O$ (where $O_2$ permits the oxidization of FeO to $Fe_2O_3$) using the thermodynamic database of Evans and Frost (2021) and Holland and Powell (2011) and the phase solution models considered are reported in Table S2 in Supporting Information S1.

Our phase equilibrium models use a *P*-*T*-X path based on the tectonic and compositional reconstructions from previous studies (Barton et al., 1987; Bebout & Barton, 1989; Grove & Bebout, 1995; Platt & Schmidt, 2024). Compositions were corrected for along-path and post-path effects using the steps outlined below. Corrected compositions for the protolith were then allowed to progress along the *P*-*T*-X until their final serpentinite compositions were met (Text S1 and Figure S1 in Supporting Information S1; Table 1).

1. $Fe^{3+}$ to $Fe^{Tot} = Fe^{3+} + Fe^{2+}$ (all in molar proportions) was reduced in the initial composition to a molar ratio of ~0.01 (derived from data in Canil et al. (1994)) to account for later serpentinization and surface oxidation. The final $Fe^{3+}$ to $Fe^{Tot}$ ratio was also fixed to match that of typical serpentinite: 0.4 (Eberhard et al., 2023) to account for surface effects such as weathering. This correction prevented the stabilization of hematite in the protolith (which happened when using the observed iron oxidation ratio). Since pure hematite is not expected in mantle rock (Haggerty, 1991, 1995), the effect of this correction was required. However, this correction did not increase the olivine/orthopyroxene ratio sufficiently to place modeled protoliths within the harzburgite field as expected from past studies of protolith lithology (Platt, 1975)
2. The initial $SiO_2$ content was reduced to 44 wt% (Bénard et al., 2021) to account for $SiO_2$ addition during serpentinization (Bebout & Barton, 1989). The final $SiO_2$ content was set to the observed proportion, assuming no post-serpentinization silica addition. This placed the protoliths within the harzburgite field.
3. The initial $H_2O$ content was reduced to 0.004 wt% (Azevedo-Vannson et al., 2021), with final water contents defined by measured LOI values.

All compositional corrections were applied to the full compositional data set (Table 1). The CaO content of all samples was also corrected using measured $P_2O_5$ contents assuming all $P_2O_5$ was contained within apatite.

The three-part geological history was modeled after current interpretations of the tectono-metamorphic history of the Catalina Schist. The first stage represents wedge cooling due to the introduction of cold subducting slab, with an isobaric temperature decrease (at 1.4 GPa; Harvey, Penniston-Dorland, et al. (2021)) from geotherm-derived pre-subduction ambient mantle temperature to the peak metamorphic temperature of the Amphibolite unit (~700 °C; Grove and Bebout (1995); Penniston-Dorland et al. (2018); Harvey, Penniston-Dorland, et al. (2021)). The second stage represents serpentinization during partial exhumation and moves linearly toward the pre-exhumation storage conditions of ~200 °C and ~0.4 GPa. The final stage represents final exhumation toward the surface and moves linearly to 100 °C and 0.1 GPa, which lies on the post-storage exhumation path for the Amphibolite unit from (Grove & Bebout, 1995). Phase changes during evolution along stage 1, stage 2 and stage 3 were computed at $N$ discrete points along their individual *P*-*T*(-X) path segments ($N = 8$ for stage 1, $N = 100$ for stage 2 and $N = 8$ for stage 3). We do not consider complete exhumation to surface conditions in our models given the limitations of phase equilibrium models at such low temperature and pressure conditions where reactions are unlikely to reach equilibrium. Given the low temperatures involved, it is reasonable to assume no significant changes in mineral assemblage during late-stage exhumation.

The compositional change described in Table 1 occurred only along the serpentinization stage and was parametrized into two linear substages, with two relative rates of compositional change controlled by how soon 70% of the final composition is reached, $PT_{0.7}$, which is the *P*-*T* condition when $C_{in} = 0.7(C_{final} - C_{proto}) + C_{proto}$ (where $C_{in}$ is the input composition, $C_{final}$ is the final composition and $C_{proto}$ is the protolith/initial composition). When $PT_{0.7}$ is set to 30% along the serpentinization path, a quicker rate of compositional change is present for the first 30% of the serpentinization path (linearly reaching 70% of the final composition) followed by a reduced rate of change (to reach the final composition) in the remaining 70% of the serpentinization path. The choice of $PT_{0.7}$ as the kink in the progression of compositional change as opposed to a different percentage of the final composition (e.g., $PT_{0.5}$) is somewhat arbitrary but does ensure that the earlier stage of compositional change corresponds to a large-scale influx of water at pressures of ~1.2–0.7 GPa (~45–25 km depth; Bebout and

Barton (1989)). Earlier and later positions of the change in the rate of compositional change along the serpentinization path were also tested ($PT_{0.7}$ = 10% and 50%).

### 3.5. Magnetic Properties

Magnetic hysteresis measurements were performed on mm-scale chips (all <13 mg) from 12 serpentine hand samples and one vein sample. In addition to the standard hysteresis parameters (saturation magnetization, $M_s$, saturation remanent magnetization, $M_{rs}$, coercivity, $H_c$, and coercivity of remanence $H_{cr}$, which can be used for Day Plots), first-order reversal curves (FORCs) were also acquired using a Princeton Measurements Corporation MicroMag Model 2900 Alternating Gradient Magnetometer (AGM) at the Department of Earth Sciences, University of Cambridge. The AGM was repeatedly calibrated using the NIST Std 2853–Magnetic moment standard #0257. Chips were weighed using a Mettler AE163 mass balance with draught shield and then mounted onto a perpendicular mounting rod using silicon grease. $M_s$ and $H_c$ were recovered from hysteresis loops, with 200–500 ms averaging time, and an applied field varying from −2 to 2 T in steps of 20 mT. $M_{rs}$ and $H_{cr}$ were found from DC demagnetization curves, with minimum 1 s averaging time, field range of 0.5 mT–1 T, and 80 points per curve distributed unevenly (exponentially larger field intervals as field strength increased). FORC measurements were acquired with 200–400 ms averaging time, saturating field between 1.5 and 2 T and measurement resolution ∼2 mT. Though Day Plots are useful for providing a quick overview of the dominant magnetic domain state within a sample, FORC diagrams produced from these measurements provide much more in-depth information on different domain state populations within each sample (Roberts et al., 2018).

FORCs were processed in FORCinel 3.08 (Harrison & Feinberg, 2008) using the VARIFORC smoothing protocol (Egli, 2013) with parameters: $Sc0 = 4$ (initial horizontal smoothing factor along the vertical ridge—i.e., at $Hc = 0$), $Sc1 = 7$ (initial horizontal smoothing factor just outside the vertical ridge region), $Sb0 = 3$ (initial vertical smoothing factor just along the horizontal ridge), $Sb1 = 7$ (initial vertical smoothing factor just outside the central ridge region) and $\lambda = 0.1$ (rate of increase in smoothing factor relative to $Hc$ moving away from the (0,0) origin) for both horizontal and vertical orientations. Principal component analysis (PCA) was performed using FORCem (Harrison et al., 2018), with endmember selection constrained by the feasibility metrics (describing how realistic the endmember is) of Harrison et al. (2018). The PCA analysis was used to unmix FORC diagram signals produced by hypothetical magnetic mineral populations with different domain state signatures and determine the contribution of each of these signatures on the observed FORC diagrams.

Temperature dependence of magnetic susceptibility measurements were made for mm-scale chips of samples M08B, 07B and M07A1 between −195 °C and 700 °C in two stages (−195 to 0 °C and 20 to 700 °C) using an AGICO KLY-5A Kappabridge (with CS-L and CS4 units) at the $M^3$Ore lab, University of St Andrews, following the procedure described in Latimer et al. (2024). The resulting temperature-susceptibility curves are used in conjunction with EDS mapping to evaluate the magnetic mineralogy of the specimens (Dunlop & Özdemir, 1997; Tarling & Hrouda, 1993). These three samples were chosen because they are the closest to the endmembers recovered from FORC analysis.

Anisotropy of magnetic susceptibility (AMS) was collected for partially serpentinized (06B, 07A, M04, M07A2, M08B) and heavily serpentinized (06A, 06C, 07B, M01A, M02, M07A1) cm-scale samples using the AGICO KLY-5A Kappabridge following methods used in previous studies such as Koopmans et al. (2022); Mattsson et al. (2021). Since our samples were much smaller than the holder (and also irregular in shape), white tack was used to stabilize them in the sample holder. A series of tests shows that the amount of white tack in the sample holder does not affect the results, with the magnetic response of the samples outweighing that of the white tack (Text S3 in Supporting Information S1). In addition to the orientation of anisotropy, bulk AMS parameters were also measured, including the degree of anisotropy, shape of the susceptibility ellipsoid and mean susceptibility.

## 4. Results

All thin-section samples contain phenocrysts (∼ 0.5–1 mm) of serpentinized amphibole and pyroxene in a matrix (∼0.05–0.3 mm grains) of cellular/polygonal serpentine, magnetite and clinochlore (Figure S3 in Supporting Information S1) with a shape-preferred orientation that defines a weak foliation (Figure 2a). In three (07A, M04, M08B) of the nine sections, relict amphibole was present (Figures 2b and 2d); in the remaining samples,

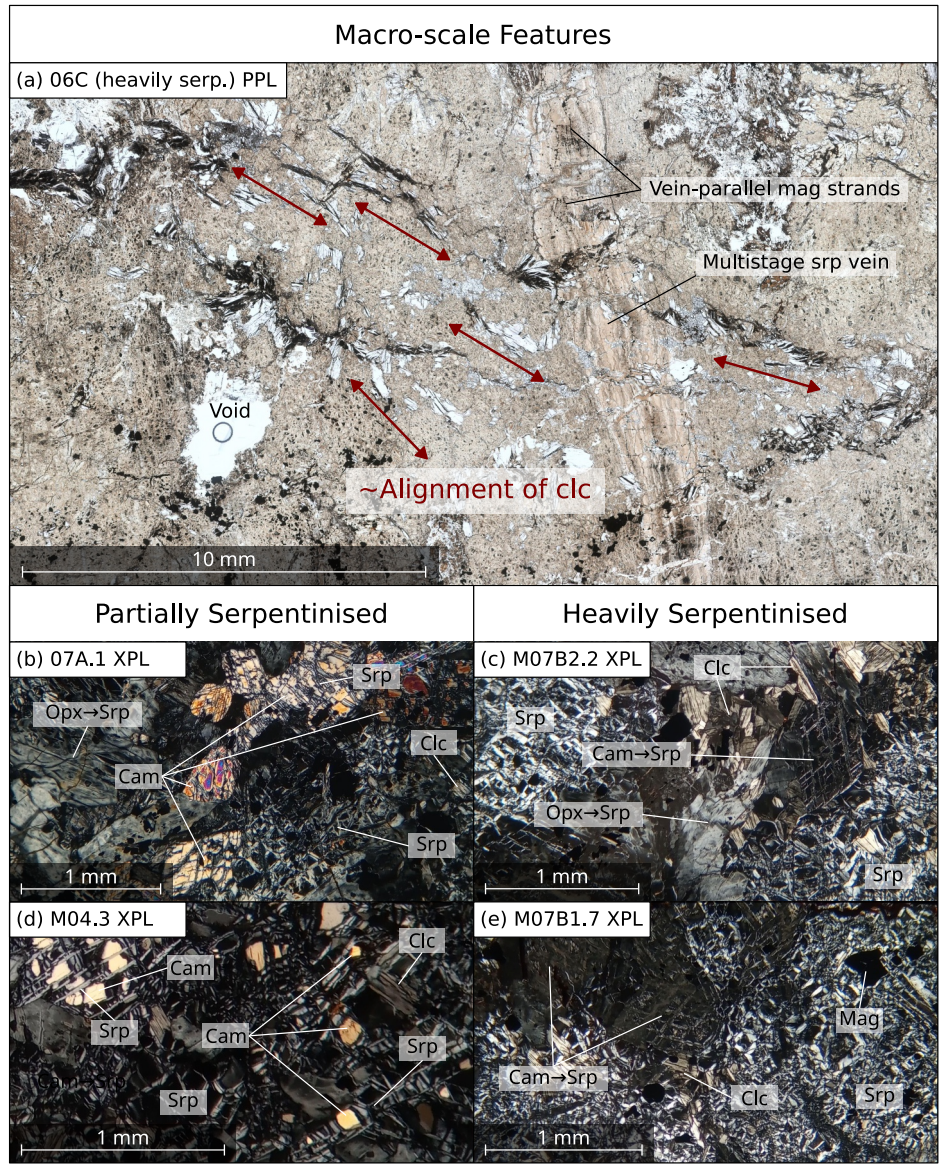


**Figure 2.** Overview of key petrographic features in the serpentinite samples (a) PPL scan of sample 06C displaying a pervasive clinochlore (clc) foliation and magnetite (mag) bearing layered/multistage vein. (b), (d) XPL photomicrographs of partially serpentinized samples containing relict clinoamphibole (cam) grains separated by serpentine (srp) meshes whose original, continuous grains were much coarser. (c), (e) XPL photomicrographs of heavily serpentinized samples with only ghost amphibole. Serpentinized orthopyroxene (opx) is distinguished from serpentinized clinoamphibole by the absence of obvious cleavage-parallel serpentine crystals that appear brightly in XPL (see also Figure 9 for a schematic of this difference). Photomicrographs taken with a Leica DM750P microscope at the Department of Earth Sciences, University of Oxford.

amphibole was completely serpentinized (or absent in the case of sample M02), leaving only ghost structures (Figures 2c and 2e). This distinction was used to categorize thin-section samples into partially and heavily serpentinized groups, respectively. No other significant mineralogical differences were observed. For hand samples, color order was found to be a better proxy for degree of serpentinization (Figure S4 in Supporting Information S1), and so used to classify these samples in terms of their extent of serpentinization.

Magnetite was observed in all samples with various associations (Figures 3 and 4a), with EPMA spot analyses revealing enrichment of the groundmass magnetites (Associations 1–3 of Figure 4a) in $Cr_2O_3$ (~10 wt%) with slightly less $Cr_2O_3$ in partially serpentinized samples (mean 8.94 ± 3.44 wt%, uncertainty is 1 standard

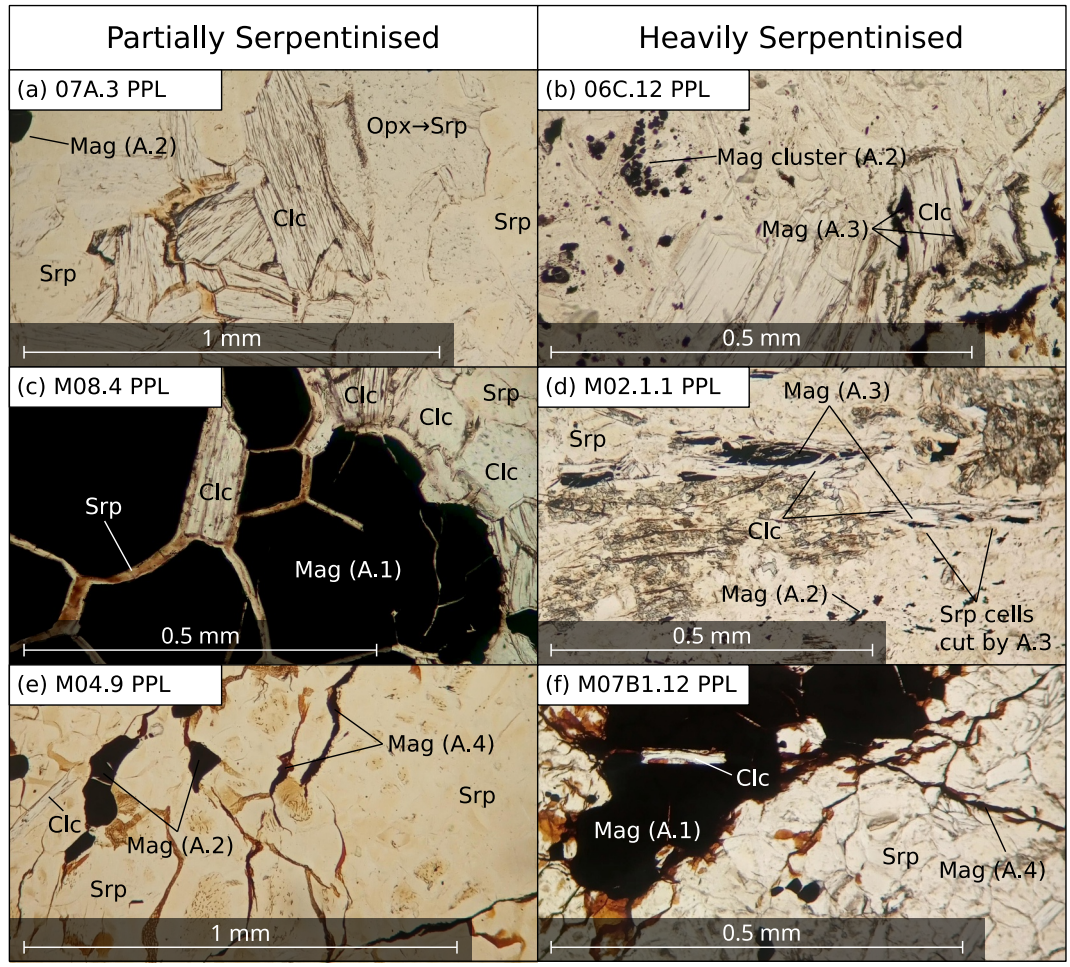


**Figure 3.** Contrasts and similarities in groundmass magnetite populations in partially versus heavily serpentinized samples. (a) Clinochlore without intergrown magnetite in the partially serpentinized sample 07A. (b) Magnetite in fine clusters in sample 06C. (b), (d) Clinochlore with intergrown magnetite in heavily serpentinized samples 06C and M02. In (d), the clinochlore-magnetite association can be seen cutting across the groundmass. (c), (f) Coarse magnetite clusters associated with clinochlore. (e), (f) Magnetite filling hairline (micron-width) fractures that cut across other grains in the groundmass. (e) Magnetite intergrown with the serpentine groundmass. Magnetite associations (based on Figure 4a) are labeled as A.n where n is the association number. Photomicrographs taken with a Leica DM750P microscope at the Department of Earth Sciences, University of Oxford.

deviation, $n = 50$) versus heavily serpentinized samples (mean 10.40 $\pm$4.84 wt%, $n = 36$), with the difference being statistically significant under a Mann-Whitney $U$ test ($p = 0.011 < 0.05$ one-tailed; see also Dataset S1, and Figure S5 in Supporting Information S1 for a boxplot comparison). As such, most of these grains have compositions within the Cr-magnetite and ferritchromite range. These two mineralogies can be expressed under the spinel system $Fe^{2+}(Fe_{1-n}Cr_n)_2O_4$ with $n$ in the range 0.1–0.2 (~6–13 wt%) for Cr-magnetite, $n < 0.1$ for magnetite and $n > 0.2$ for ferritchromite (Hodel et al., 2020). Under these definitions, the major element chemistry indicates that in the partially serpentinized group, 5 grain measurements are consistent with magnetite, 36 with Cr-magnetite and 9 with ferritchromite; and in the heavily serpentinized group, 7 with magnetite, 16 with Cr-magnetite and 13 with ferritchromite. The majority of grains in both the partially and heavily serpentinized sample groups are Cr-magnetite, though ferritchromite is more prevalent in the heavily serpentinized samples compared to in the partially serpentinized samples.

$TiO_2$ content was generally low in magnetite from both partially (1.16 $\pm$ 2.30 wt%, $n = 50$) and heavily (0.25 $\pm$0.10 wt%, $n = 36$) serpentinized thin sections. The high mean $TiO_2$ content in the partially serpentinized samples is a result of four (out of a sample total of 30—i.e., 13%) rare Ti-rich magnetite grains measured in sample M08B (with no clear optical differences to the other magnetite grains in reflected light, or differences in

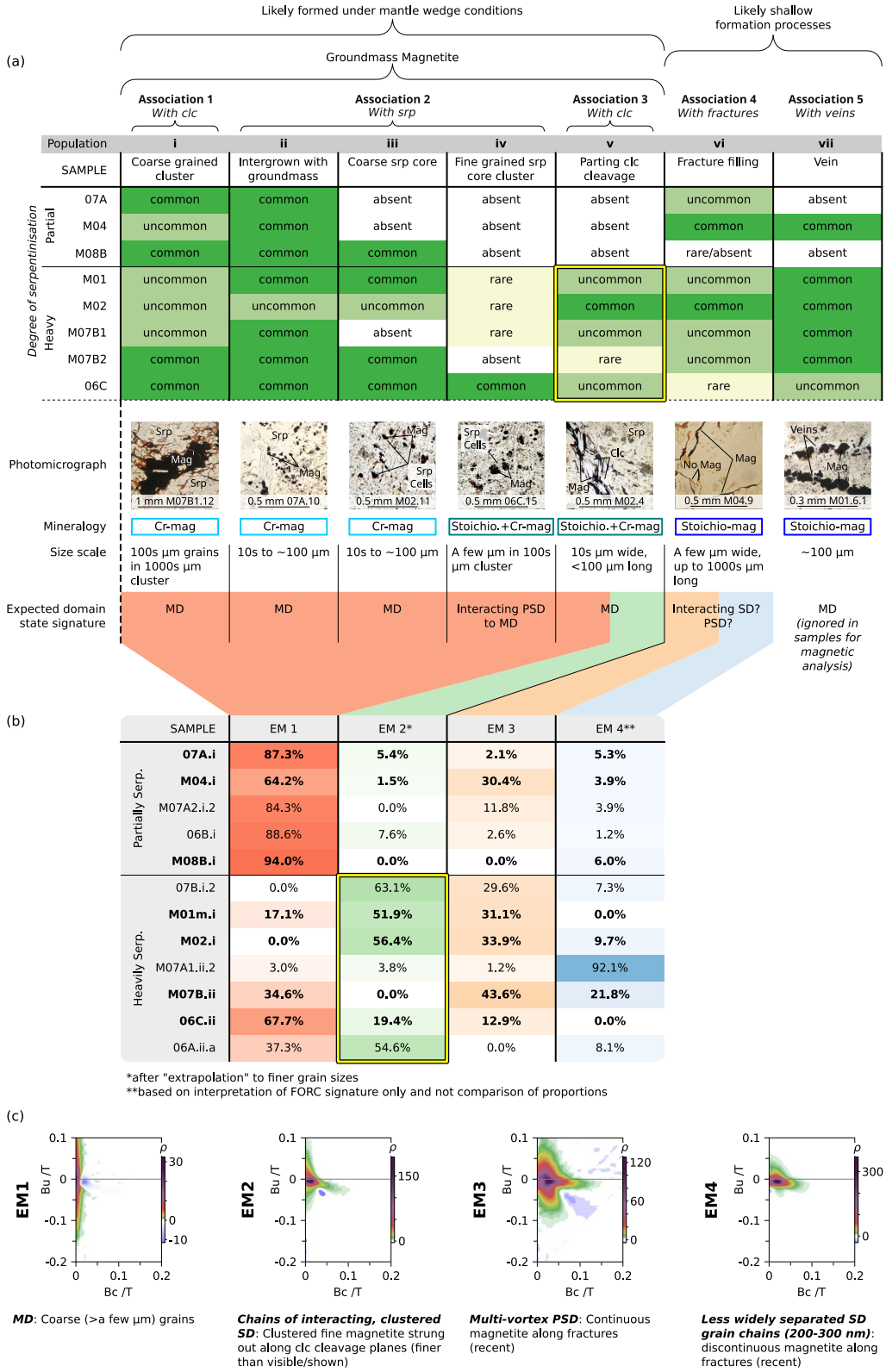
(a)
Likely formed under mantle wedge conditions
Likely shallow formation processes
Groundmass Magnetite
Association 1 With clc
Association 2 With srp
Association 3 With clc
Association 4 With fractures
Association 5 With veins
Population i ii iii iv v vi vii
SAMPLE Coarse grained cluster | Intergrown with groundmass | Coarse srp core | Fine grained srp core cluster | Parting clc cleavage | Fracture filling | Vein
Degree of serpentinisation
Partial
07A common common absent absent absent uncommon absent
M04 uncommon common absent absent absent common common
M08B common common common absent absent rare/absent absent
Heavy
M01 uncommon common common rare uncommon uncommon common
M02 uncommon uncommon uncommon rare common common common
M07B1 uncommon common absent rare uncommon uncommon common
M07B2 common common common absent rare uncommon common
06C common common common common uncommon rare uncommon
Photomicrograph
1 mm M07B1.12
0.5 mm 07A.10
0.5 mm M02.11
0.5 mm 06C.15
0.5 mm M02.4
0.5 mm M04.9
0.3 mm M01.6.1
Mineralogy
Cr-mag | Cr-mag | Cr-mag | Stoichio.+Cr-mag | Stoichio.+Cr-mag | Stoichio-mag | Stoichio-mag
Size scale
100s µm grains in 1000s µm cluster | 10s to ~100 µm | 10s to ~100 µm | A few µm in 100s µm cluster | 10s µm wide, <100 µm long | A few µm wide, up to 1000s µm long | ~100 µm
Expected domain state signature
MD | MD | MD | Interacting PSD to MD | MD | Interacting SD? PSD? | MD (ignored in samples for magnetic analysis)
(b)
SAMPLE EM 1 EM 2* EM 3 EM 4**
Partially Serp.
07A.i 87.3% 5.4% 2.1% 5.3%
M04.i 64.2% 1.5% 30.4% 3.9%
M07A2.i.2 84.3% 0.0% 11.8% 3.9%
06B.i 88.6% 7.6% 2.6% 1.2%
M08B.i 94.0% 0.0% 0.0% 6.0%
Heavily Serp.
07B.i.2 0.0% 63.1% 29.6% 7.3%
M01m.i 17.1% 51.9% 31.1% 0.0%
M02.i 0.0% 56.4% 33.9% 9.7%
M07A1.ii.2 3.0% 3.8% 1.2% 92.1%
M07B.ii 34.6% 0.0% 43.6% 21.8%
06C.ii 67.7% 19.4% 12.9% 0.0%
06A.ii.a 37.3% 54.6% 0.0% 8.1%
*after "extrapolation" to finer grain sizes
**based on interpretation of FORC signature only and not comparison of proportions
(c)
EM1
EM2
EM3
EM4
Bu /T
Bc /T
MD: Coarse (>a few µm) grains
Chains of interacting, clustered SD: Clustered fine magnetite strung out along clc cleavage planes (finer than visible/shown)
Multi-vortex PSD: Continuous magnetite along fractures (recent)
Less widely separated SD grain chains (200-300 nm): discontinuous magnetite along fractures (recent)

**Figure 4.**

Fe:O molar ratio from EPMA data; Dataset S1). The low $TiO_2$ content in both sample groups is even more apparent when comparing medians, which are 0.30 and 0.25 wt% $TiO_2$for partially and heavily serpentinized samples, respectively. No clear petrographical relations were observed between the location of these four grains and other features such as fractures, veins or pores within the thin section.

The high Cr content of most groundmass magnetites is further supported by EDS imaging (Figures 5a and 5b). Although hairline (micron-width) fracture-filling magnetite (Association 4 of Figure 4a) was too fine to image through EPMA, EDS images revealed their stoichiometric nature, uncontaminated by Cr or Ti (Figure 5a). A magnetite vein was imaged in sample M01A and found to be stoichiometric in nature (Figure 5c). Magnetite grains are commonly anhedral in the groundmass (Figure 3e), though occasional examples of subhedral to euhedral grains were observed in some veins (most notably in M01A) as well as in very fine clusters (Figure 3b).

FORC PCA (Figures 4b and 4c; Text S4 in Supporting Information S1) revealed that four endmembers (in PCA space defined by three principal components) were sufficient to explain 98.75% of observed variance between data-derived FORC diagrams (Figure S7 in Supporting Information S1): Endmember (EM) 1 is a peak elongated along the internal field ($Bu$) axis at near-zero coercivity ($Bc$); EM2 is a peak at $Bc = 0.013$, $Bu = -0.002$; EM3 is a trilobate signature with peak at $Bc = 0.025$, $Bu = 0$; EM4 is similar in form to EM2 but shifted to higher $Bc$, with peak at $Bc = 0.018$, $Bu = -0.002$. Two data-derived FORC diagrams (M04.i, Figure S8 in Supporting Information S1, and M07A2.i.2) contained two clear FORC signatures (i.e., two peaks), supporting the suitability of PCA analysis (i.e., providing clear evidence that at least some FORC diagrams represent mixtures of multiple signatures). By comparing temperature-susceptibility curves and magnetite population occurrences to the proportion of endmember FORCs in the respective sample, each endmember can be interpreted in the context of the magnetite populations (Figure 6, Section 5.1.2).

The higher temperature (20–700 °C) segments of the temperature-susceptibility curves also display clear differences (Figure 6) between the three samples that have very different petrographic and/or FORC properties (Figure 4). The low temperature segments of the curves are dominated by an artifact of $N_2$ vaporization rather than magnetic properties of the samples and so are not considered here (see Figure S2 in Supporting Information S1 for the full temperature–susceptibility plots that show this as well as the cooling curves). Sample M08B, which is dominated by magnetite populations i-iii in thin section and EM1 in its magnetic signature, has a narrow Curie temperature range around 520 °C. Sample 07B's magnetic signature is mostly characterized by EM2, but with appreciable contribution from EM3 as well, and has a broad Curie temperature range lying mostly between 540 and 580 °C (with an upper limit of ~ 620 °C). Sample M07A1's magnetic signature is dominated by EM4, and has a narrow Curie temperature around 580 °C preceded by a Hopkinson peak. All three samples display a change in gradient at ~300 °C along the heating curve (Figure 6; which is absent on the cooling curve; Figure S2 in Supporting Information S1). This change in gradient is more pronounced for the heavily serpentinized samples, with the slope changing sign about a peak.

Due to the weakness of the foliation, the presence of many vein sets associated with exhumation, and the non-oriented nature of the samples, it is unsuitable to compare the anisotropy orientations of the partially versus heavily serpentinized sample groups. Comparison of bulk AMS parameters (degree of anisotropy, shape of the susceptibility ellipsoid and mean susceptibility) revealed no clear differences between the partially versus heavily serpentinized sample groups (Figure S10 in Supporting Information S1).

**Figure 4.** Comparing petrographically observed magnetite populations and first-order reversal curve (FORC) PCA-determined magnetic grain populations. (a) Table of magnetite population abundances for samples grouped by their petrographically determined serpentinization level. Photomicrograph examples of the population morphology/relationships are shown and magnetite mineralogy determined by energy dispersive spectroscopy observation are noted. The size and morphology typifying each population are used to predict the domain signature associated with each population. Though this table contains both groundmass magnetite (Associations 1–3), fracture-filling magnetite (Association 4) and vein magnetite (Association 5), veins were avoided for the magnetic analyses so there's no link between Association 5 and any of the endmember FORC signatures. (b) The proportions of the four endmember FORC signatures (as constrained by feasibility metrics) within observed FORC diagrams, with the samples from which the observations were made grouped by their petrographically observed- and color-inferred serpentinization level. Bold samples are those that had a corresponding thin section sample and thus present in (a). A link between the abundance of petrographic Association 3 (magnetite + late clinochlore) and occurrence of magnetic Endmember 2 only in heavily serpentinized samples is highlighted. (c) The four modeled endmember FORC signatures, alongside interpretations of the magnetic grain populations they represent. Photomicrographs taken with a Leica DM750P microscope at the Department of Earth Sciences, University of Oxford.

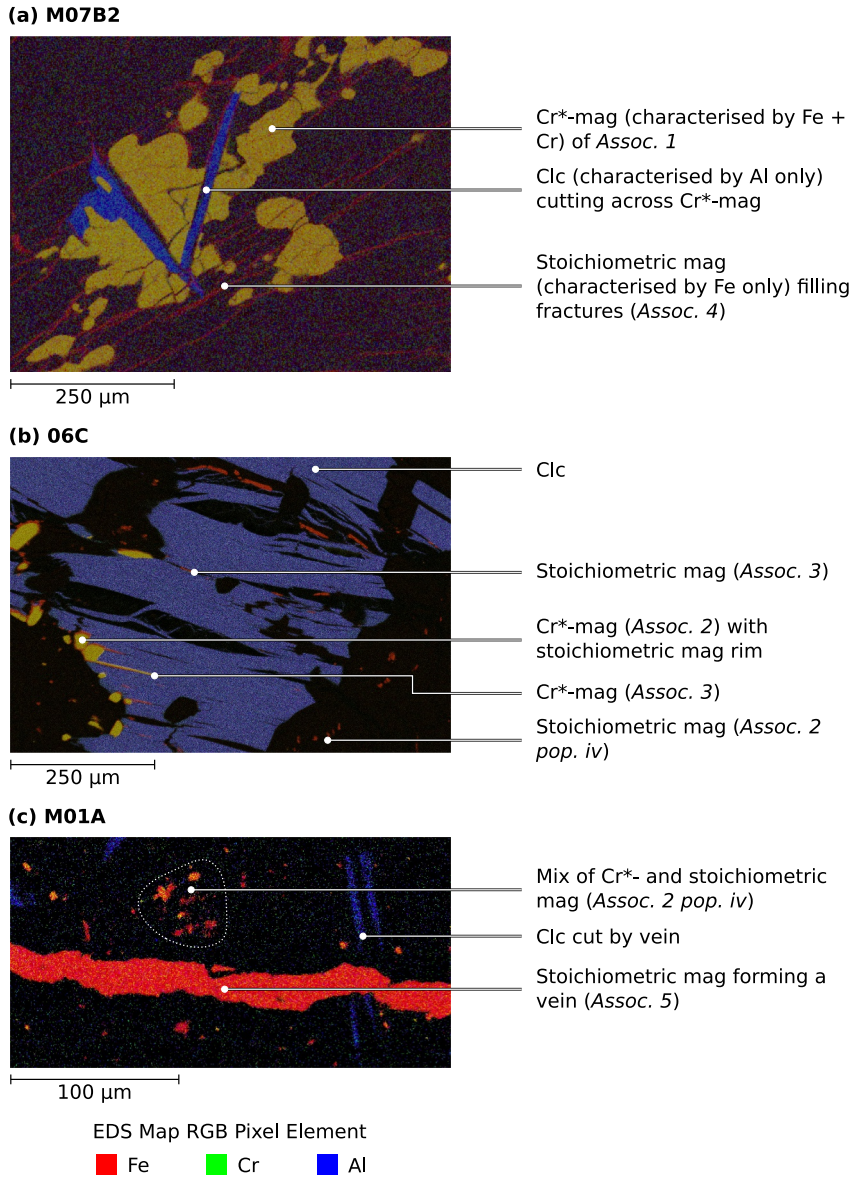


**Figure 5.** RGB Composite energy dispersive spectroscopy (EDS) maps (Fe, Cr, Al for the RGB channels respectively) showing compositions of the magnetite associations as identified in Figures 3 and 4a and observed in three samples: (a) M07B2 (b) 06C (c) M01A. The phases highlighted in color by this composite map are Cr-enriched magnetite (Cr*-mag, which are treated as Cr-magnetites in discussions of petrography for simplicity) in yellow (Fe and Cr), stoichiometric magnetite in red (just Fe), and clinochlore in blue (Al). The regions without any of these elements are mostly serpentinite. For all the composite EDS maps investigating magnetite compositions in M01A, 06C, 07A, M07B2, and M08B, see Figure S6 in Supporting Information S1; for individual elemental EDS maps, see Fish et al. (2025).

### 4.1. Partially Serpentinized Samples

Partially serpentinized thin sections (07A, M04, M08B) are dominated by serpentine (55%–75% by area) and contain between 2% and 10% relict tremolite (with phase identification based on analysis of EPMA compositional data; Text S5 in Supporting Information S1), and 2%–10% serpentinized amphibole (mostly as meshes around relict grains), 3%–15% serpentinized pyroxene, 10% clinochlore and <3% magnetite (Figures 2b and 2d). Hand samples of these three sections had densities in the range 2.37–2.57 g $cm^{-3}$. The samples had color values <89, with the two darkest (lowest value) samples (M04 and 07A) also being the two densest samples in the full hand sample collection (see Figure S4 in Supporting Information S1).

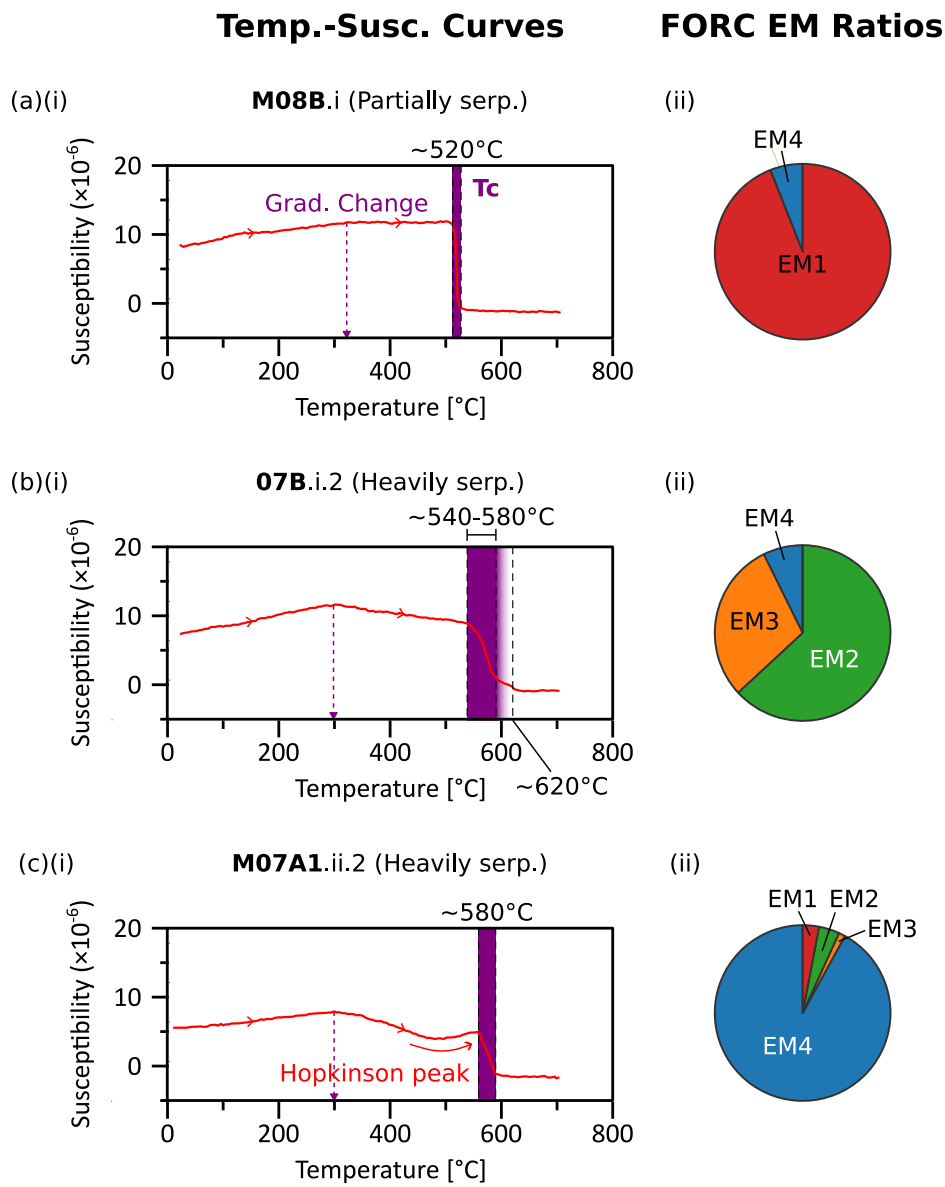


**Figure 6.** Comparison between the (i) high temperature (20–700 °C) temperature-susceptibility curves along the heating path and (ii) normalized endmember first-order reversal curve (FORC) ratios for samples (a) M08B, (b) 07B and (c) M07A1. The Curie temperature (Tc) ranges are drawn on in purple. The cooling paths display the same Curie temperature ranges and are not shown here for clarity. For the full temperature versus susceptibility plots that include cooling paths (as well as the low temperature segments), see Figure S2 in Supporting Information S1. Numerical ratios of the endmember FORCs for each sample can be seen in Figure 4.

A range of magnetite morphologies were identified in the partially serpentinized sections, and grouped by their silicate mineral associations. Compositionally, the magnetites of these associations were found to be predominantly Cr-magnetites based on EPMA and EDS analysis on magnetite grains in samples 07A and M08B (Figure S6 in Supporting Information S1). Coarse Cr-magnetite grains (of order 0.1 mm diameter) that formed mm-scale clusters with individual grains separated by thin serpentine walls were associated with rare clinochlore grains (Figures 3c and 4a, Association 1/Population i). Individual medium to coarse (of order 0.01–0.1 mm diameter) Cr-magnetite grains were found to be associated with the serpentine groundmass, either as intergrown grains (Figures 3e and 4a, Association 2/Population ii) or in the cores of serpentine cells. Pure, stoichiometric magnetite was also observed to fill hairline fractures that cut across the groundmass for distances up to a few mm (Figure 4a, Association 4/Population vi)—though this population was not observed in sample M08B. The bulk rock magnetic

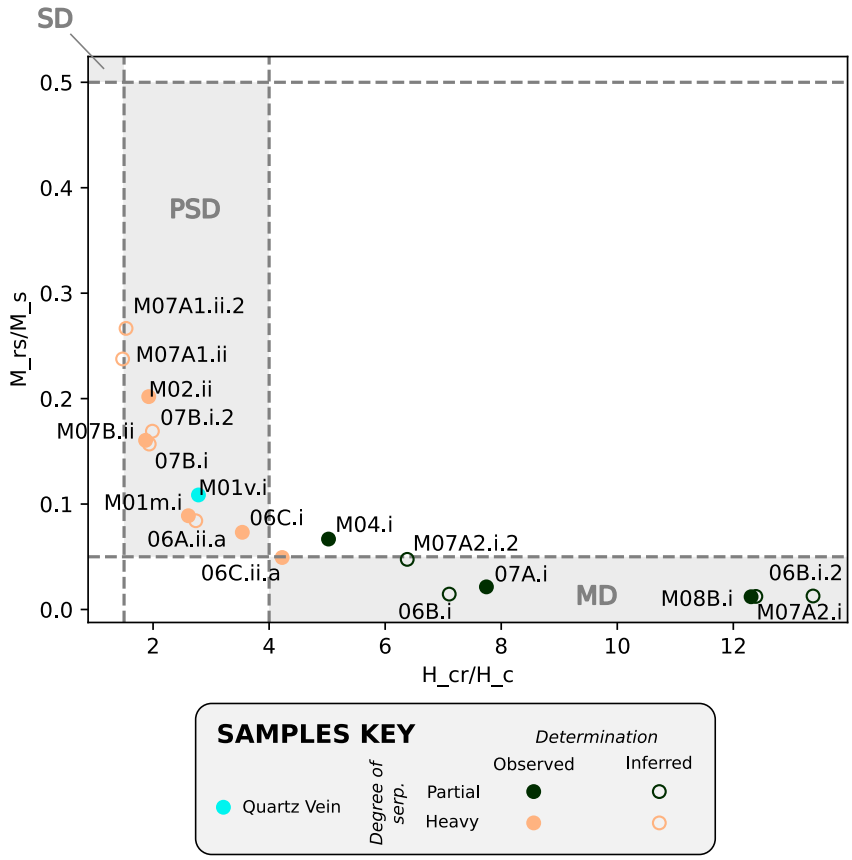


**Figure 7.** Day Plot showing a clear difference in the bulk-rock magnetic properties of partially versus heavily serpentinized samples. Partially serpentinized samples lie mostly within the MD region, whereas heavily serpentinized samples lie mostly within the PSD region. The degree of serpentinization is "observed" if it is based on thin section observations (with the complete serpentinization of amphibole used to define heavily serpentinized samples), and "inferred" if based on hand sample color ordering. Domain state region boundaries after Day et al. (1977).

signatures of partially serpentinized samples all have a $H_{cr}/H_c$ ratio >4.5 and lie in or near the multidomain region of the Day Plot (Figure 7). Of the four synthetic endmember FORC signatures identified by PCA, these samples are dominated by EM 1 and 3 (Figure 4b).

### 4.2. Heavily Serpentinized Samples

Heavily serpentinized thin sections (06C, M01A, M02, M07B1, M07B2) have groundmasses dominated by serpentine (40%–90% by area) and contain between 1% and 20% serpentinized amphibole, 1%–20% serpentinized pyroxene (Figures 2c–2e), ∼2%–15% clinochlore and <∼3% Cr-magnetite. Silica is also present in some samples, forming discrete colloform veins in M01A and being more distributed throughout the groundmass in 06C (Figures S11 and S12 in Supporting Information S1 respectively). Samples classified as heavily serpentinized from thin section analysis (06C, M01A, M02, M07B) had overlapping densities with the partially serpentinized samples but with a slightly lighter (smaller) range between 2.28 and 2.46 g $cm^{-3}$. However, these samples all had color values >94, with the lightest (06C) also having the lowest density (see Figure S4 in Supporting Information S1).

In addition to the magnetite populations observed in the partially serpentinized thin sections, two additional populations were observed in the heavily serpentinized thin sections: finer magnetite (a few μm) clusters (100 μm) in the cores of serpentine cells that were most common in 06C (Figure 3b; Association 2/Population iii) and medium to coarse (on the order of 10s–100 μm long with aspect ratios around 4:1), cleavage-parallel lenticular pure magnetite (Figures 3b and 3d; Association 3/Population v) intergrown with pervasively foliated clinochlore (Figure 2e). The weakly foliated clinochlore of Association 3 cuts across the groundmass, which hosts

Association 2 (Figures 2a and 3d). Additionally, EBSD mapping of a coarse magnetite cluster in the heavily serpentinized sample M07B1 revealed non-uniform orientations in the individual grains (Figure S13 in Supporting Information S1). Compositionally, the magnetite populations that were also present in the partially serpentinized samples are still Cr-magnetite (i.e., Association 1 and populations ii and iii of Association 2). However, the magnetite populations that are found exclusively in the heavily serpentinized samples (i.e., population iv of Association 2 and Association 3) appear to be mostly a combination of Cr-magnetite and stoichiometric magnetite (Figures 5b and 5c). Furthermore, some Cr-magnetites of Association 2 were observed to be rimmed by stoichiometric magnetite (Figure 5b), indicating that the stoichiometric magnetite formed later than the Cr-magnetite.

Heavily serpentinized samples all have bulk rock magnetic signatures with a $H_{cr}/H_c$ ratio <4.5 and lie in or near the pseudo-single domain region of the Day Plot (Figure 7). Of the four FORC signatures identified by PCA, these samples are dominated by EM2 and EM3. EM4 is also present in broadly higher proportions than in partially serpentinized samples, most notably so in sample M07A1, whose FORC diagram comprises >90% EM4 (Figure 4b).

### 4.3. Phase Equilibrium Modeling

Phase equilibrium models for both partially (07A) and heavily (06B, 07B, M02) serpentinized samples produced protolith- and final mineral assemblages that are consistent with each other (except the heavily serpentinized sample 06C), with little modal mineral change in the first (cooling) or third (final exhumation) stage (e.g., Figures 8a and 8b, Figures S14 and S15 in Supporting Information S1 for all of these models). There is much more mineralogical change during the serpentinization stage of these phase equilibrium models, which occurs after the initial cooling-related metamorphic stage. In the model for 06C, voluminous talc (~20 vol%) is predicted in the final assemblage, which is not observed in thin section. This is likely caused by post-"final-exhumation" silica enrichment of 06C outside of the model parameters, which is supported by the presence of free quartz disseminated throughout the thin section. Despite much along-path compositional change in the serpentinization and partial exhumation stage, the models (again except 06C) produced major mineral assemblages broadly similar to observed (particularly in serpentine and clinochlore, but not amphibole). As such, the serpentinization and final exhumation stages for 06C are not considered further here.

#### 4.3.1. Initial (Protolith) and Final Mineralogies

The predicted protoliths of all samples (e.g., Figure 8b) primarily comprise olivine (>70 vol%), orthopyroxene (~15–20 vol%) and clinopyroxene (~5–10 vol%), with magnetite being absent. Cr-bearing minerals were also absent due to limitations of the data input to the phase equilibrium models. Modeled final mineral assemblages comprise 75%–80% serpentine and <10% clinochlore. The models predict generation of voluminous (~10%–15%) free fluid ($H_2O$) in the final mineral assemblages, which may suggest that a fraction of the LOI ($H_2O$) observed in bulk/XRF compositions was added outside of the *P-T*-X domain considered by the phase equilibrium models (i.e., water added after the *P-T*-X endpoint in the model) or represents a different volatile. Minor iron oxides are present (~2.5 vol.%) either as magnetite or hematite (in which case talc is also stable).

#### 4.3.2. Mineralogy Changes Along the Serpentinization Path

Clinoamphibole (mostly tremolite), which is present in low amounts in the protolith (<1 vol.%) increases significantly at the start of the serpentinization stage (700 °C, 14 kbar) to <2.5 vol.%, but is absent by the end of the serpentinization stage. Clinochlore also experiences a dramatic increase in stability from absence in the protolith to ~15 vol.% at the start of the serpentinization path before reducing to ~ 1 vol% (in the case of the partially serpentinized 07A) or 0 vol% (heavily serpentinized M02, 06B, and 07B) shortly after (this clinochlore volume reduction happens around 570–600 °C, 11.5–12 kbar). The sharp decrease in clinochlore volume coincides with a sharp increase in antigorite volume and decrease in forsterite volume at ~625 °C, 12.5 kbar. Clinochlore stability increases gradually after ~575 °C, 11.5 kbar.

The appearance of magnetite occurs around or after the first peak in clinochlore stability (675 °C, 13.5 kbar). The volume of magnetite increases approximately linearly throughout the decrease in volume of clinochlore/increase in volume of serpentine. The rate of magnetite production decreases throughout the renewed increase in volume of later clinochlore. Two of the four models (06B and M02) predict that magnetite is converted to hematite in the

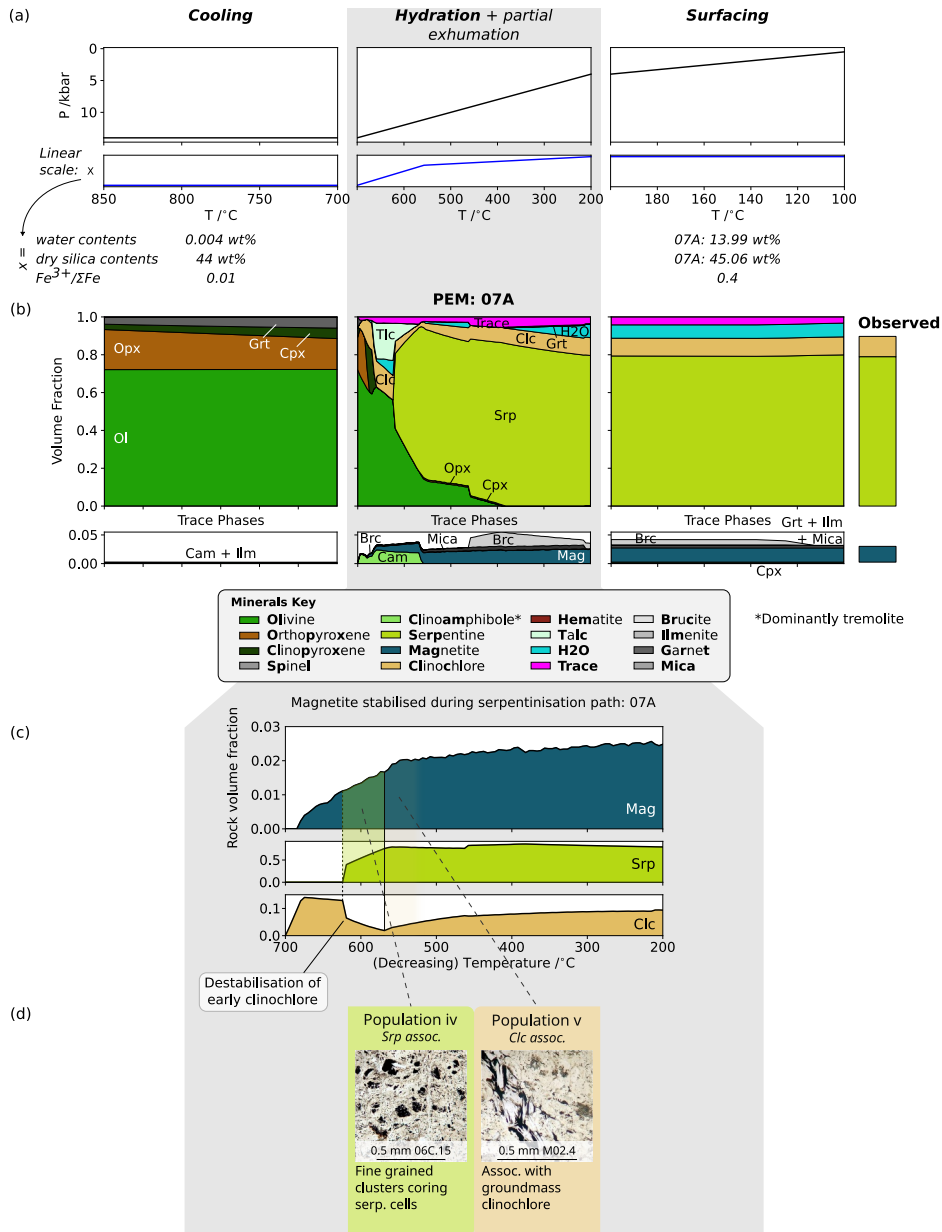


**Figure 8.** Results of phase equilibrium modeling (PEM) of the composition of sample 07A. (a) Input three-stage *P-T*-X path (cooling, serpentinization and partial exhumation, and surfacing) representing the serpentinite/amphibolite's geological history (see Figure 1d). (b) Results of PEM showing the predicted stable mineral assemblage at each point along the *P-T*-X path vertically above in (a), with relative time progressing from left to right. (c) Comparison between magnetite and major silicate vol% stabilized during the serpentinization path to infer chronological connections to different magnetite associations. (d) Photomicrographs of the three magnetite associations observed in thin section. Photomicrographs taken with a Leica DM750P microscope at the Department of Earth Sciences, University of Oxford. Mineral name abbreviations from (Whitney & Evans, 2010): Ol—olivine, Opx—orthopyroxene, Cpx—clinopyroxene, Spl—spinel, Cam—clinoamphibole, Srp—serpentine, Mag—magnetite, Clc—clinochlore, Hem—hematite, Tlc—talc, Brc—brucite, Ilm—ilmenite, Grt—garnet.

later half of the model, coincident with the increase in volume of talc (in the case of 06B) or prior to this (in the case of M02) the increase in volume of talc.

Changing the initial rate of compositional change (by varying $PT_{0.7}$) affects the rate and magnitude of magnetite volume change. However, the key directional features remain: two major increases in clinochlore separated by

clinochlore volume decrease/serpentine volume increase, all occurring synchronously with magnetite growth (Figures S16 and S17 in Supporting Information S1 for $PT_{0.7} = 10\%$, Figures S18 and S19 in Supporting Information S1 for $PT_{0.7} = 50\%$), suggesting that the magnetite–silicate associations predicted by the model are robust.

### 4.4. Vein Geochemical Profiling

All veins investigated in M01A, two out of four in M02 and two out of five in 06C (Figure 8avii and e.g., Figure 2a) were found to have geochemical profiles consistent with formation in an open fracture (Text S6 in Supporting Information S1; Oliver and Bons (2001)). This collection of veins included quartz ± magnetite and serpentine ± magnetite veins. The remaining two veins of M02 were found to be multistage, with a serpentine vein postdating a quartz + magnetite vein. Due to interference between the profile signatures of the two separate veins, it was difficult to infer a formation mechanism. The remaining three veins of 06C comprised serpentine and had geochemical profiles consistent with a diffusive, closed-system formation mechanism (wallrock mimicry profiles; e.g., Figure S22 in Supporting Information S1). Though two of these veins also contained magnetite, the segmented occurrence of magnetite in these veins suggested it wasn't formed synchronously with vein serpentinite. As such, there's no evidence for magnetite formed in a diffusive, closed-system vein.

## 5. Discussion

### 5.1. Magnetite Populations

#### 5.1.1. Petrology

Between the magnetite populations, three modes of formation are identified. The most common magnetite composition is Cr-magnetite, present in the groundmasses of both partially and heavily serpentinized rock (populations i-iii; Figures 5a and 5b). These Cr-magnetites are interpreted as resulting from the alteration of Cr-spinel in mantle material under high fluid:rock ratios and amphibolite-grade metamorphic conditions (Farahat, 2008; Hodel et al., 2020). This is consistent with these samples being from the Amphibolite Unit of the Santa Catalina Schist, with peak metamorphic P-T conditions of 650–730 °C and 1.34–1.44 GPa (Harvey, Penniston-Dorland, et al., 2021; Penniston-Dorland et al., 2018), which corresponds to a depth of ∼45–50 km assuming a ∼0.3 GPa/10 km lithostatic pressure gradient. Since the ultramafic samples of the Amphibolite Unit are interpreted to represent mantle wedge material (Platt, 1975; Sorensen, 1988), this temperature would have likely been reached through cooling from an ambient mantle temperature of 720–800 °C (assuming an approximate geothermal gradient of 16 °C/km for the upper 50 km of the lithosphere; Figure 6d of Manea and Manea (2011)) in order to facilitate amphibolite metamorphism. A subduction environment would not only fulfill this cooling requirement through the depression of wedge temperatures by the descending slab, but also the high fluid:rock ratio necessary for the conversion of original Cr-spinel to Cr-magnetite. With EBSD mapping of the coarse magnetite cluster in the M07B1 revealing non-uniform orientations in the individual grains (such that the cluster is a collection of individual grains rather than a single large grain that was later split apart), the original Cr-spinels likely had a grain size similar to the individual grains that form the cluster, that is, up to a few hundred microns diameter.

The mixtures of Cr-magnetite and stoichiometric magnetite (population iv and v) are likely associated at least in part with a subsequent serpentinization stage, which are expressed in the heavily serpentinized samples and not the partially serpentinized samples. The Cr-magnetite in these populations is interpreted to have also formed by earlier conversion of Cr-spinel to Cr-magnetite compared to the formation of the stoichiometric magnetite as evidenced by the observation of stoichiometric magnetite rims around Cr-magnetite grains in Figure 5b. The stoichiometric magnetite rims (and isolated grains away from Cr-magnetite grains) are interpreted to have formed as a result of serpentinization, which released and subsequently oxidized iron from ferromagnesian silicates (Saad, 1969). The PEM results provide some insight into the order of formation of the stoichiometric magnetite components of population iv (fine magnetite clusters associated with serpentinite) and population v (lenticular magnetite found between clinochlore foliation planes) during the serpentinization stage (Figure 8d), though it should be noted that the PEMs model pure magnetite (Cr was measured as a trace element without valence information and so could not be included as an oxide). Stoichiometric magnetite formation is initially associated with serpentine stabilization (population iv) and then with the gradual stabilization of clinochlore (population v). Since the PEMs predicts that magnetite formation occurs relatively early on in the serpentinization stage (and at

pressures >10 kbar, corresponding to depths > ∼ 33 km), the models also demonstrate that formation of this stoichiometric magnetite occurred under subduction zone conditions rather than post-exhumation. The restriction of this groundmass-based stoichiometric magnetite to heavily serpentinized rocks likely arises due to their greater extent of serpentinization in the mantle wedge (as opposed to later exhumation-related processes), which permitted greater iron release through the breakdown/conversion of ferromagnesian silicates to serpentinite.

The ubiquitous hairline fracture-filling stoichiometric magnetite (population vi/Association 4) is interpreted to correspond to a later geological event (e.g., exhumation) based on cross-cutting relations (Figures 3e, 3f, 4a and 5a). Geochemical profiles across the similarly ubiquitous veins suggest that all vein magnetite (population vii/Association 5; e.g., Figures 2a and 4a-vii) was formed in either open fractures or after diffusive, closed system veins had already formed. Furthermore, almost all of these veins cut across the groundmass (Figure S21 in Supporting Information S1). Therefore, we take the cautious approach of not interpreting any fracture-filling or vein magnetites in the context of mantle wedge processes.

#### 5.1.2. Magnetic Properties

EM1 is a clear multidomain (MD) magnetite signature (Roberts et al., 2014), which dominates the FORC diagrams of partially serpentinized samples and is also present in significant proportions in heavily serpentinized samples. The temperature-susceptibility curve of sample M08B (narrow 520 °C Curie temperature; Figure 6a), which is dominated by EM1, is consistent with Cr-magnetite with 6–13 wt% $Cr_2O_3$(Hodel et al., 2020). As such, the occurrence of EM1 is not only consistent with the occurrence of Cr-magnetite populations i-iii (Figures 4a and 4b), but also the composition of those magnetite populations.

EM2 has a PSD-like signature with a peak at slightly negative *Bu* offset, which is interpreted to represent interacting chains of magnetic grains (Harrison & Lascu, 2014). Additionally, the vertical spreading approaching zero coercivity (i.e., the left vertical axis) and triangular shape suggests closely packed interacting single-domain magnetic grains (Harrison et al. (2019), Figure 3e of Sridhar et al. (2021)). As such, EM2 is interpreted to represent strung-out chains of clustered SD (or fine PSD) magnetite grains. Large contributions from the EM2 signature are restricted to FORC diagrams measured on heavily serpentinized samples. With Cr + stoichiometric (mixed) magnetite population v being present in appreciable proportions exclusively in heavily serpentinized samples and also possessing chained configurations along clinochlore cleavage planes (albeit at much coarser scales than for SD magnetite), it's not unreasonable to expect a connection between EM2 and perhaps the finer equivalent of the observed Cr + stoichiometric magnetite population v. This is somewhat supported by the temperature-susceptibility curve of sample 07B, whose FORC magnetic signature predominantly comprises EM2: the broad Curie temperature range between 540 and 580 °C suggests a mixture of Cr-magnetite and stoichiometric magnetite. However, such chains of fine grains (sub-micron scale; Butler and Banerjee (1975)) or fine grain clusters have been too fine to observe using the imaging methods of this study and so this connection is highly uncertain.

EM4 is similar to EM2 with regards to the negative *Bu* offset of its peak, with a smaller vertical spread in its peak interpreted to reflect less strongly interacting magnetite grains. EM4 is uncommon and only present as the dominant signature in M07A1, which has no corresponding thin section sample. With the only other feature that could host SD magnetite chains being the hairline fractures, EM4 is tentatively associated with submicron-scale magnetite that may be present discontinuously along these fractures. This would be consistent with the thermal demagnetization curve representing EM4 (which dominates sample M07A1). A Curie temperature of 580 °C preceded by a Hopkinson peak indicates the presence of relatively pure/stoichiometric magnetite, which is observed to fill these hairline fractures (though mostly in a continuous manner).

EM3 is interpreted to be a multivortex PSD signal (Roberts et al., 2014), and is present in a similar range of proportions in partially and heavily serpentinized samples. In addition to their similar occurrences across the sample collection, the flattened (micron-width) and highly elongate nature of the fracture-filling magnetites is consistent with a multivortex PSD signal (Lascu et al., 2018). As such EM3 is connected to stoichiometric magnetite population vi with some confidence. Although EM3 was not present in majorly dominant proportions in the FORC samples, the confident connection to population vi suggests it would likely have a temperature-susceptibility curve representative of magnetite.

Some second order features of the temperature-susceptibility plots are also noteworthy, namely the change in gradient at ~300 °C and presence of a magnetic grain population with a Curie temperature of 620 °C in sample 07B (Figure 6). The change in gradient is tentatively connected to the presence of ferritchromite, with the positive slope <~300°C potentially reflecting destabilization of ferritchromite into maghemite and the negative slope >~300°C resulting from subsequent maghemite destabilization (Hodel et al., 2020). This connection to ferritchromite would also explain the difference in the temperature-susceptibility slope change between the partially and heavily serpentinized samples: EPMA spot analyses suggests that ferritchromite is more common in the heavily serpentinized samples, and so their effect on the overall rock magnetic properties is greater. The absence of a negative slope >~300 °C for the partially serpentinized sample could arise from the dominance of Cr-magnetite's signature over those of destabilizing maghemite. Despite this hypothesized effect of ferritchromite being more prominent in the heavily serpentinized samples, Cr-magnetite and stoichiometric magnetite remain the dominant magnetic mineralogies. As such, we interpret Cr-magnetite and/or stoichiometric magnetite populations as the dominant control on derived FORC-PCA endmembers. Similarly, while temperature-susceptibility curves for 07B indicate a small population of grains with a Curie temperature of 620 °C, tentatively interpreted as being Ti-bearing hematite/titanohematite (Fabian et al., 2008), these grains were not identified in quantitative SEM (EPMA) analysis and are thus thought to be minor. This is supported by a more general rarity of Ti-bearing iron oxides, being observed only infrequently (as magnetites) in the thin section of M08B. In addition, since titanohematite has a lower magnetic susceptibility than magnetite, it is unlikely that this population of magnetic minerals is reflected in the FORC diagrams (or FORC endmember proportions). As such, this population is not considered in further analysis.

### 5.2. Effect of Metamorphism and Serpentinization on Mantle Wedge Rock Properties

We have shown that the extent of metamorphism and serpentinization affects both the mineralogical composition and the nature of magnetite populations and their resulting magnetic properties (Figure 9). This is due to variations in the associations of magnetite grains with silicate phases, leading to distinct magnetic signatures in heavily and partially serpentinized mantle-wedge samples. In contrast to the results of Saad (1969) for the effect of variable serpentinization on rock magnetic properties in a relatively undeformed serpentinized ultramafic intrusion, increasing the extent of serpentinization results in the growth of finer populations of magnetite grains (namely interacting clusters of SD grains strung out in a chain, which may be related to the clinochlore-associated magnetite of population v).

The degree-of-serpentinization classification scheme adopted here is robust for both petrographic and rock magnetic characterization of recovered samples (Figure 9). Partially and heavily serpentinized thin sections were distinguished by the presence or absence of relict clinoamphibole (tremolite), respectively, with additional hand samples classified by color and density (where the heavily serpentinized rocks are lighter in color and generally less dense; Figure 9). Rock magnetic analyses also indicate that partially serpentinized samples have magnetic signals dominated by MD magnetic grains (populations i-iii), whereas heavily serpentinized samples also contain appreciable contributions from interacting clustered SD grains (SD equivalent of population v), which gives rise to a whole-rock PSD signature (Figure 7). Since different magnetite populations have different compositions, the magnetic mineralogy of partially versus heavily serpentinized samples also differs. Partially serpentinized samples contain Cr-magnetite formed by the metamorphism of Cr-spinel (populations i-iii). Heavily serpentinized samples contain stoichiometric magnetite formed by serpentinization reactions under mantle conditions (populations iv and v) in addition to Cr-magnetite. Both partially and heavily serpentinized samples also contains stoichiometric magnetite filling hairline fractures and veins (populations vi and vii, respectively) associated with exhumation post-dating subduction.

### 5.3. Subduction Zone Magnetic Structure

Combining our petrographic and rock magnetic analyses with the extent of serpentinization recovered from geological and seismic observations in subduction zones (Epstein et al., 2024; Reynard, 2013; Xia et al., 2015), allows us to hypothesize how different geological processes can influence the magnetic structure of the mantle wedge and their implications on subduction zone CPD patterns.

The greater proportions of EM2 in the FORC diagrams produced from heavily serpentinized samples suggests that their magnetic properties is dominated by the magnetic signature of chains of clustered sub-micron scale SD

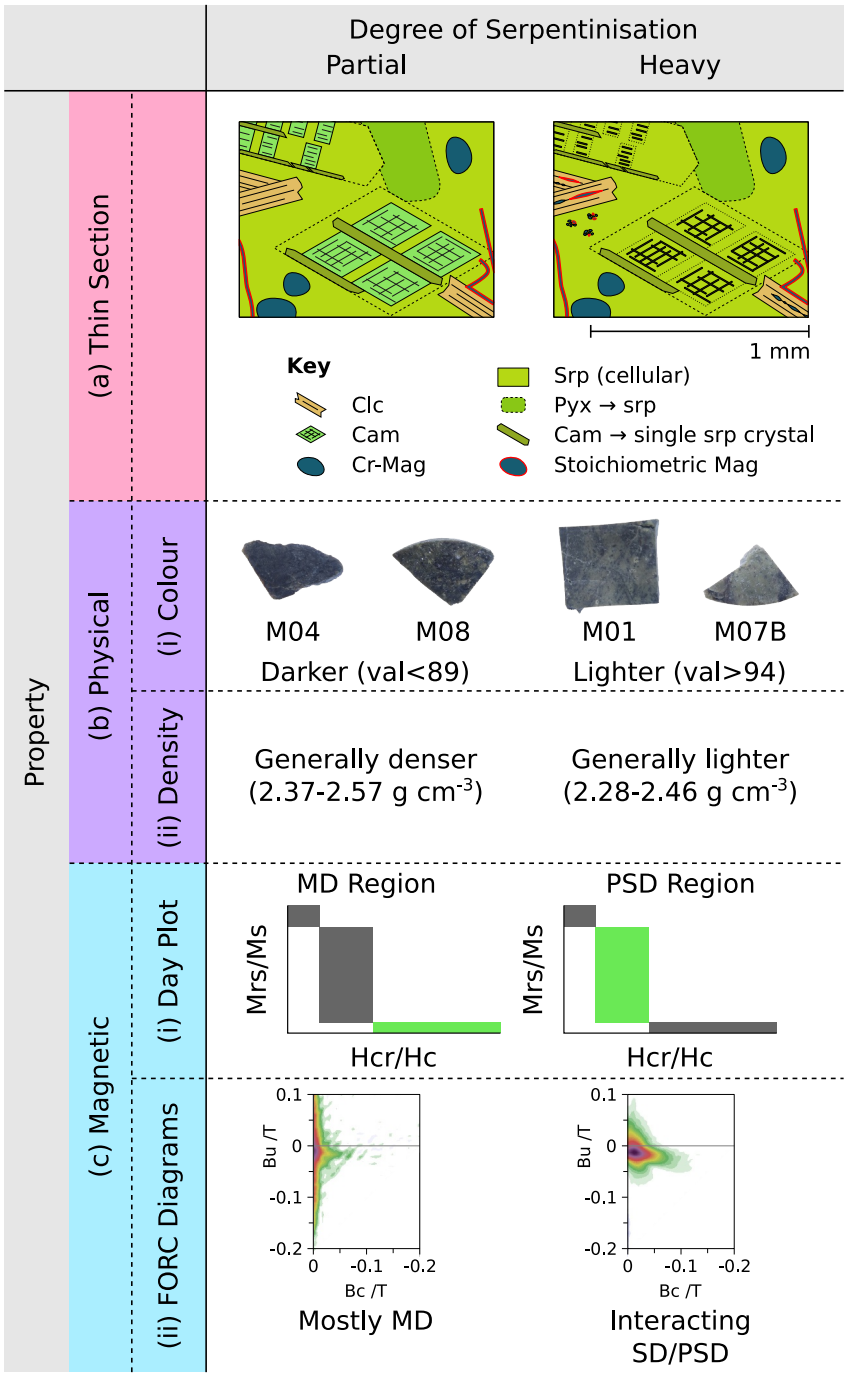


**Figure 9.** Comparison between the (a) petrographical, (b) bulk physical and (c) magnetic properties of partially versus heavily serpentinized samples. (a) Schematic thin section views showing the key petrographical differences between partially and heavily serpentinized samples. Partially serpentinized samples contain relict clinoamphibole (Cam) and no magnetite associated with late-stage clinochlore (no early clinochlore is shown in the schematics). (b) Partially serpentinized hand samples are (i) darker (reflected by a lower RGB value) compared to heavily serpentinized samples, and (ii) generally denser. (c) Partially serpentinized samples contain a greater proportion of multidomain magnetic grains to pseudo-single domain ones, with this property observed in both (i) Day Plots and (ii) first-order reversal curve diagrams.

magnetite associated, perhaps related to the coarser 10–100 micron scale magnetite strung out along clinochlore cleavage planes. These strung out chains would be expected to have a direction of anisotropy parallel to the long axis of the chain (Sagnotti, 2020), that is, parallel to the weak foliation defined by the clinochlore cleavage planes.

As such, it would be expected that within the mantle, heavily serpentinized samples would be more anisotropic compared to the partially serpentinized samples, whose magnetic properties are dominated by the relatively equant MD magnetite grains of EM1. However, the field relations in Santa Catalina are not clear enough for the orientation of the clinochlore fabrics to be related to the orientation of the original subduction interface with certainty. Furthermore, AMS measurements reveal no noticeable differences in bulk anisotropy properties between partially and heavily serpentinized samples. This may be a result of interference in the anisotropy signal by the fracture-filling magnetite or vein magnetite which were avoided in the mm-scale FORC samples but unavoidable in the cm-scale AMS samples. As both the fracture-filling and vein magnetite likely formed at depths too shallow to be representative of mantle wedge conditions, it is not possible to preclude an increase in bulk anisotropy from partially to heavily serpentinized rock within the mantle (i.e., in the absence of exhumation-related fractures/veins). In order to explore the influence of magnetic fabrics on CPD, it is recommended that future studies should focus on the effect of any shearing-parallel magnetic fabrics in geological contexts where petrological fabrics can be directly related to subduction zone geometry.

Though not confirmed by AMS data, the possibility that heavily serpentinized samples may contain an anisotropic magnetite population could provide and additional explanation to the CPD shallowing at the corner of the mantle wedge observed by Manea and Manea (2011). Magnetic anisotropy in EM2 if hosted in the cleavage planes of subduction-parallel foliated clinochlore grains would likely possess a different orientation to the ambient magnetic field. Depending on their relative orientations, this magnetic anisotropy could amplify or dampen the ambient field when measured on earth's surface, hampering a simple interpretation of CPDs. Based on the serpentinization models of Reynard (2013); Xia et al. (2015), any magnetic anisotropy hosted by subduction foliation would have the strongest effect on surface magnetic measurements where the subduction interface intersects the Moho of the overlying plate (i.e., the corner of the mantle wedge, where strongly sheared mantle wedge just above the subduction zone is shallowest). And if the magnetic anisotropy were misaligned to the local Earth magnetic field, then this effect might explain a locally shallowed CPD within a broader region of partially serpentinized mantle wedge dominated by EM1 MD magnetite with magnetic moments aligned to the local Earth magnetic field (see Figure S23 in Supporting Information S1 for a diagrammatic representation of this hypothesis).

While we cannot confirm that magnetic anisotropy plays a significant role in the interpretations of CPDs, we highlight that significant compositional differences in magnetic mineralogy between partially and heavily serpentinized rocks may give rise to CPD variations due the varying Curie temperature of each magnetite population. The presence of Cr-magnetite in these wedge-sourced mantle samples indicates that metamorphism of Cr-spinel to Cr-magnetite is able to occur in a tectonic environment outside of ophiolites (Farahat, 2008; Hodel et al., 2020), and that serpentinization is not the only process that generated significant magnetite in mantle wedges. Furthermore, this metamorphic mode of (Cr-)magnetite formation occurs in both partially and heavily serpentinized mantle samples. In contrast, serpentinization-related stoichiometric magnetite formation only occurs in the heavily serpentinized samples. Taken in the context of schematic extent of serpentinization maps in subduction zones after Reynard (2013) and Xia et al. (2015), and a schematic simplification of one of the subduction zone thermal models of Manea and Manea (2011), this magnetic mineralogy contrast might also contribute to a mismatch between the shape of the 580 °C isotherm and the CPD observed by Manea and Manea (2011).

A sufficient fluid:rock ratio for Cr-spinel to Cr-magnetite metamorphism is proxied by the extent of serpentinization, and since the metamorphic transformation was observed in even the partially serpentinized samples this region spans a large portion of the wedge. The intersection of the amphibolite and fluid:rock regions is the region over which Cr-spinel to Cr-magnetite transformation is expected, with the partially serpentinized part predicted to contain only Cr-magnetite (Figures 10b-iii) and the heavily serpentinized part just above the subduction interface predicted to contain both Cr-magnetite and stoichiometric magnetite (Figures 10b-ii). At depths shallower than this region (i.e., under sub-amphibolite conditions), the formation of Cr-magnetite is predicted to be less extensive relative to stoichiometric magnetite formation through serpentinization reactions, and so the shallowest region of the wedge corner is predicted to have a magnetic mineralogy dominated by stoichiometric magnetite (Figures 10b-i). Here, the shallow limit of amphibolite metamorphism in the wedge is taken as being controlled by temperature (i.e., the minimum amphibolite facies temperature of 500°C isotherm and the deep limit by the peak pressure of the Amphibolite Unit of up to 1.44 GPa (Harvey, Penniston-Dorland, et al., 2021; Penniston-Dorland et al., 2018), which corresponds to a depth of ∼ 50 km.

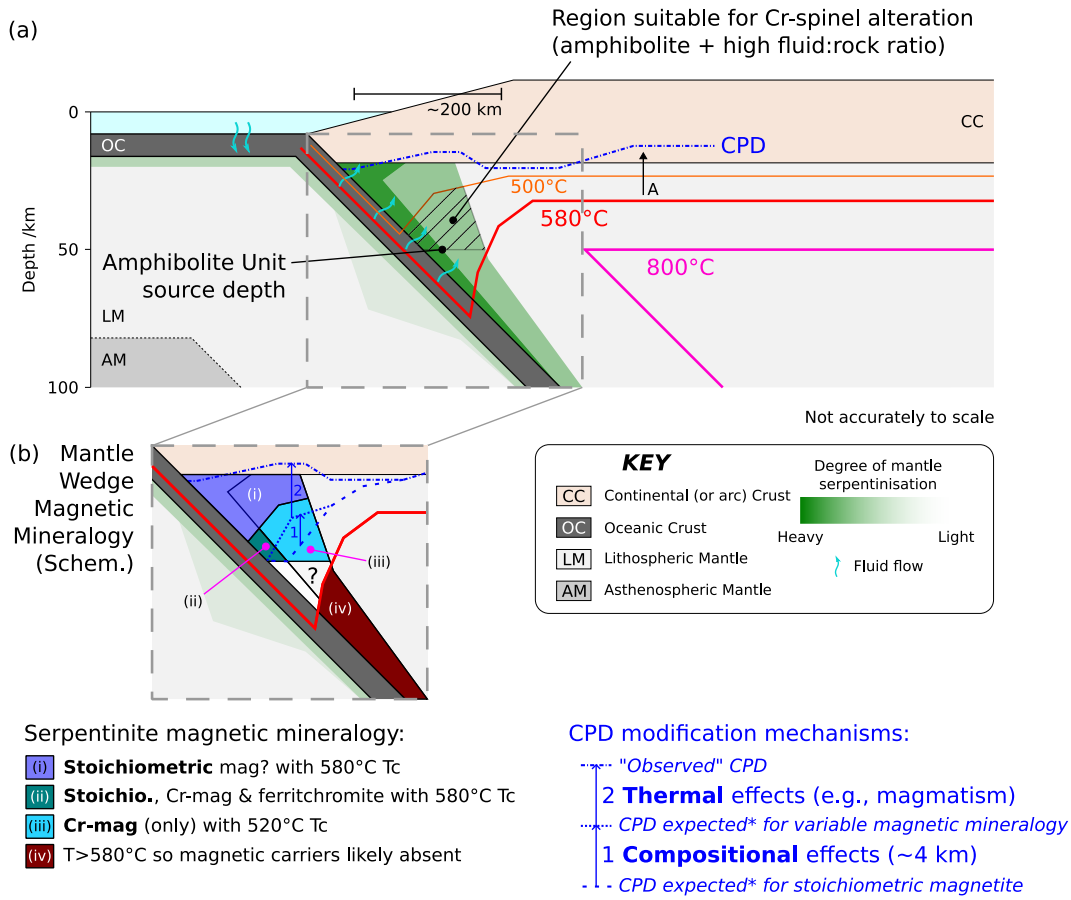


**Figure 10.** Possible magnetic mineralogy model for mantle wedge magnetic structure linking observations and interpretations ranging from regional scale (e.g., seismology) to sample scale (this study). (a) Schematic of features informed by regional-scale observations, including extent of serpentinization and Curie point depth (CPD) depth. The region within which Cr-spinel to Cr-magnetite metamorphism is predicted to be possible and extensive is marked with diagonal black lines. The Amphibolite Unit source depth (up to 50 km) is also marked on. The arrow A represents shallowing of the baseline CPD relative to the 580 °C isotherm, perhaps due to some combination of systematic thermal model and/or CPD method uncertainties. (b) Predicted magnetic mineralogies and largest Curie temperature (Tc) of each assemblage (corresponding to the mineral in bold). An observed CPD pattern and expected (*in a highly schematic sense) CPD patterns for a mantle wedge containing only stoichiometric magnetite as the magnetic mineralogy (i.e., parallel to the 580 °C isotherm) and a mantle wedge with variable magnetic mineralogy (i.e., with the CPD shallowing where Cr-magnetite is the magnetic carrier) are plotted to illustrate the two CPD shallowing mechanisms. The isotherms and CPD pattern are schematically after Manea and Manea (2011). Serpentinization pattern and dimensions after Figure 1 of Reynard (2013) and Figures 5a–5d and 6k–6n of Xia et al. (2015).

Due to its greater proximity to the surface, shallower stoichiometric magnetite should dominate the wedge's regional-scale magnetic signal (deeper CPD). Below this part of the wedge, the Cr-magnetite dominated partially serpentinized wedge adjacent to mixed Cr-magnetite/stoichiometric magnetite bearing heavily serpentinized wedge (just above the interface) may exert a smaller-scale effect on the CPD. Since Cr-magnetite has a lower Curie temperature (520 °C) than stoichiometric magnetite (580 °C), with the 60 °C difference corresponding to a CPD depth difference of ~4 km (Text S7 in Supporting Information S1), this predicted configuration of magnetic mineralogies would result in a shallower CPD than expected for a mantle wedge containing just stoichiometric magnetite (as the magnetic mineralogy). However, this composition-related shallowing of the CPD is unlikely to shallow the CPD to above the base of the magnetic layer, so thermal effects (Manea & Manea, 2011) likely remain the major control on CPD patterns around subduction zones (Figure 10b). Regardless, this result does suggest that lateral variations in subduction zone CPDs do not need to mirror lateral variations in the 580°C Curie isotherm of stoichiometric magnetite.

It is clear from the differences in the magnetic mineralogies and domain state populations present in partially versus heavily serpentinized mantle wedge material that mantle wedge magnetization is not uniform in subduction zone settings. Instead, a combination of the degree of serpentinization, fluid:rock ratios, P-T conditions and potentially also the proximity to the high-strain subduction interface (and orientation of any resultant shear fabrics relative to the ambient magnetic field) can affect the magnetic properties of mantle wedge material. As a result, extra care should be taken when interpreting variations in CPD around subduction zones as a response to temperature, and to keep large-scale differences in the composition of magnetic phases and perhaps also the presence of petrofabrics in mind.

In order to investigate the effect of magnetic mineralogy on mantle wedge magnetic structure further, the fluid availability and distribution in mantle wedges should be quantified for subduction zones on an individual basis (e.g., Epstein et al., 2024). The distribution and extent of fluid availability can provide insight into spatial variations of serpentinization degree, and by extension the degree of transformation of Cr-spinel to Cr-magnetite when combined with wedge P-T models. With wedge fluid distribution in subduction zones being primarily imaged by passive seismic methods (Reynard, 2013; van Keken & Wilson, 2023; Xia et al., 2015), greater instrumentation above mantle wedges would increase seismic imaging resolution and thus facilitate better wedge hydration models for individual subduction zones.

## 6. Conclusions

Mantle wedge serpentinites from Santa Catalina Island/Pimu'nga, California, USA, display petrographic and magnetic properties that vary with degree of serpentinization and extent of metamorphism. All samples contain MD Cr-magnetite grains formed by complete replacement of Cr-spinel during amphibolite-grade regional metamorphism brought on by mantle wedge cooling, and in the presence of abundant fluids, Heavily serpentinized samples contain these grains in addition to other magnetic minerals (stoichiometric magnetite and ferritchromite), whereas partially serpentinized samples contain almost exclusively Cr-magnetite as the magnetic mineralogy. Cr-magnetite has a lower Curie temperature (520°C) than stoichiometric magnetite (580°C), so if Cr-magnetite is interpreted as magnetite, then a CPD may be misinterpreted as being hotter than it actually should be. As a result, lateral variations in the misfit between subduction zone CPDs relative to the 580°C stoichiometric magnetite Curie isotherm can overestimate thermal effects on CPD shallowing, with temperature differences of 60°C and associated shallowing (dependent on the geothermal gradient) able to arise from these compositional effects alone.

A combination of petrology, PEM and magnetic measurements permits the identification of magnetite populations and their corresponding magnetic properties associated with late exhumation. By removing these post-exhumation signatures from our analyses, we can compare the magnetic properties of partially and heavily serpentinized samples in a mantle wedge context. Partially serpentinized rocks contain relict clinoamphibole, are darker in color and generally denser, and have a mantle wedge magnetic mineralogy dominated by coarse Cr-magnetite grains. Heavily serpentinized rocks contain amphibole that is fully serpentinized, are lighter in color and generally less dense, and have a mantle wedge magnetic mineralogy that contains stoichiometric magnetite in addition to Cr-magnetite (and ferritchromite), with the possibility of sub-micron scale magnetite grains being aligned to a foliation. The distribution of partially and heavily serpentinized rock under amphibolite facies conditions in the mantle wedge can influence the apparent magnetic signal of the mantle wedge observed at the surface, and could shallow the CPD above a subduction zone independently from thermal effects.

We highlight the importance of considering both the composition of magnetic minerals and their alignment to petrofabrics when using magnetic signals to interpret the thermal structure of subduction zones in North America, and perhaps also more globally. Since fluid distribution controls both the degree of serpentinization and the volumetric extent of Cr-spinel to Cr-magnetite transformation, and this distribution varies between subduction zones, individualized imaging of mantle wedge fluid distributions lead the way for more careful consideration of large-scale compositional variation in mantle magnetic mineralogy and permit more accurate interpretations of subduction zone CPD patterns.

## Acronyms

**CPD** Curie point depth

**EBSD** Electron backscatter diffraction

| | |
|---|---|
| **EDS** | Energy dispersive spectroscopy |
| **EPMA** | Electron probe microanalyzer |
| **MD** | Multidomain |
| **PEM** | Phase equilibrium modeling |
| **PPL** | Plane polarized light |
| **PSD** | Pseudo-single domain |
| **RL** | Reflected light |
| **SD** | Single domain |
| **SEM** | Scanning electron microscope |
| **TL** | Transmitted light |
| **XPL** | Cross polarized light |
| **XRF** | X-ray fluorescence |
| $PT_{0.7}$ | *P-T* condition when $C_{in} = 0.7\left(C_{final} - C_{proto}\right) + C_{proto}$ is reached (where $C$ is composition and the subscript denotes *in*put, *proto*lith (initial) and *final*). |
| ***P-T*-X** | Pressure-Temperature-Composition |
| **AGM** | Alternating gradient magnetometer |
| **EM** | Endmember |
| **FORC** | First order reversal curve |
| **PCA** | Principal component analysis |

## Conflict of Interest

The authors declare no conflicts of interest relevant to this study.

## Data Availability Statement

Phase equilibrium modeling, magnetic data plotting, geochemical analysis, petrographic image analysis and vein profiling code (in the form of Jupyter Notebooks) can be accessed via Li (2025). This code is licensed under GNU GPLv3. Supporting data can be accessed on Zenodo: micropetrographic images can be accessed via Li, Palin, and Nichols (2024), and reflected light scans via Li and Nichols (2024a); EPMA spot analysis location via Li and Nichols (2024b); vein EDS imagery via Lindquist and Li (2024); a comprehensive collection of vein profiles and maps derived from this EDS imagery via Li, Nichols, and Lindquist (2024); AGM magnetic data and the code used to process it (combined into one Igor Pro project file) via Li et al. (2025); AMS stereonets (by sample) via Han et al. (2025). This data is licensed under CC BY 4.0. Additional magnetite EDS imagery (including element maps) can be accessed via Fish et al. (2025).

**Acknowledgments**
The authors gratefully acknowledge the constructive and valuable comments of Fátima Martín-Hernández and an anonymous reviewer throughout the review process. YL would like to acknowledge funding from the Department of Earth Sciences and Exeter College (University of Oxford). CBC and CION acknowledge funding from Royal Society International Exchange Grant IES \\R2 \\222169. We thank Krzysztof Sokol and Andrew Matzen for assistance with microscopy and microprobe/EPMA data collection. Part of this work was conducted at the Molecular Analysis Facility, a National Nanotechnology Coordinated Infrastructure (NNCI) site at the University of Washington, which is supported in part by funds from the National Science Foundation (awards NNCI-2025489, NNCI-1542101), the Molecular Engineering & Sciences Institute, and the Clean Energy Institute.

## References

Azevedo-Vannson, S., France, L., Ingrin, J., & Chazot, G. (2021). Mantle metasomatic influence on water contents in continental lithosphere: New constraints from garnet pyroxenite xenoliths (France & Cameroon volcanic provinces). *Chemical Geology*, *575*, 120257. https://doi.org/10.1016/j.chemgeo.2021.120257

Barton, M. D., Bebout, G. E., & Sorensen, S. S. (1987). *Isotopic Constraints on the Geochemical Evolution of an Ultramafic Subduction Zone Melange: Catalina Schist Terrane, California*. In (Vol. 68, p. 1525). American Geophysical Union (AGU). https://doi.org/10.1029/eo068i044p01209

Bebout, G. E., & Barton, M. D. (1989). Fluid flow and metasomatism in a subduction zone hydrothermal system: Catalina Schist terrane, California. *Geology*, *17*(11), 976–980. https://doi.org/10.1130/0091-7613(1989)017<0976:FFAMIA>2.3.CO;2

Bebout, G. E., & Barton, M. D. (2002). Tectonic and metasomatic mixing in a high-T, subduction-zone mélange—insights into the geochemical evolution of the slab–mantle interface. *Chemical Geology*, *187*(1–2), 79–106. https://doi.org/10.1016/s0009-2541(02)00019-0

Bénard, A., Müntener, O., Pilet, S., Arculus, R. J., & Nebel, O. (2021). Silica-rich spinel harzburgite residues formed by fractional hybridization-melting of the intra-oceanic supra-subduction zone mantle: New evidence from TUBAF seamount peridotites. *Geochimica et Cosmochimica Acta*, *293*, 477–506. https://doi.org/10.1016/j.gca.2020.11.001

Bhattacharyya, B. K., & Leu, L.-K. (1975). Analysis of magnetic anomalies over Yellowstone National Park: Mapping of Curie point isothermal surface for geothermal reconnaissance. *Journal of Geophysical Research*, *80*(32), 4461–4465. https://doi.org/10.1029/jb080i032p04461

Blakely, R. J. (1988). Curie temperature isotherm analysis and tectonic implications of aeromagnetic data from Nevada. *Journal of Geophysical Research*, *93*(B10), 11817–11832. https://doi.org/10.1029/jb093ib10p11817

Blakely, R. J., Brocher, T. M., & Wells, R. E. (2005). Subduction-zone magnetic anomalies and implications for hydrated forearc mantle. *Geology*, *33*(6), 445–448. https://doi.org/10.1130/G21447.1

Bouligand, C., Glen, J. M., & Blakely, R. J. (2009). Mapping Curie temperature depth in the Western United States with a fractal model for crustal magnetization. *Journal of Geophysical Research*, *114*(B11), B11104. https://doi.org/10.1029/2009JB006494

Bowles, J. A., Lappe, S. C., Jackson, M. J., Arenholz, E., & van der Laan, G. (2019). Curie temperature enhancement and cation ordering in titanomagnetites: Evidence from magnetic properties, XMCD, and Mössbauer spectroscopy. *Geochemistry, Geophysics, Geosystems*, *20*(5), 2272–2289. https://doi.org/10.1029/2019GC008217

Briggs, R. W., Sieh, K., Meltzner, A. J., Natawidjaja, D., Galetzka, J., Suwargadi, B., et al. (2006). Deformation and slip along the Sunda Megathrust in the great 2005 Nias-Simeulue earthquake. *Science*, *311*(5769), 1897–1901. https://doi.org/10.1126/science.1122602

Butler, R. F., & Banerjee, S. K. (1975). Theoretical single-domain grain size range in magnetite and titanomagnetite. *Journal of Geophysical Research*, *80*(29), 4049–4058. https://doi.org/10.1029/jb080i029p04049

Canil, D., Rudnick, N. D. P. R., & Carswell, W. D. M. (1994). Ferric iron in peridotites and mantle oxidation states (Vol. *123*). https://doi.org/10.1016/0012-821X(94)90268-2

Connard, G., Couch, R., & Gemperle, M. (1983). Analysis of aeromagnetic measurements from the Cascade Range in central Oregon. *Geophysics*, *48*(3), 376–390. https://doi.org/10.1190/1.1441476

Day, R., Fuller, M., & Schmidt, V. A. (1977). Hysteresis properties of titanomagnetites: Grain-size and compositional dependence. *Physics of the Earth and Planetary Interiors*, *13*(4), 260–267. https://doi.org/10.1016/0031-9201(77)90108-X

de Capitani, C., & Brown, T. H. (1987). The computation of chemical equilibrium in complex systems containing non-ideal solutions. *Geochimica et Cosmochimica Acta*, *51*(10), 2639–2652. https://doi.org/10.1016/0016-7037(87)90145-1

de Capitani, C., & Petrakakis, K. (2010). The computation of equilibrium assemblage diagrams with Theriak/Domino software. *American Mineralogist*, *95*(7), 1006–1016. https://doi.org/10.2138/am.2010.3354

Dunlop, D. J., & Özdemir, O. (1997). *Rock Magnetism: Fundamentals and Frontiers*. Cambridge University Press. https://doi.org/10.1017/cbo9780511612794

Dunlop, D. J., & Özdemir, Ö. (2015). Magnetizations in rocks and minerals. In *Treatise on geophysics* (pp. 255–308). Elsevier.

Eberhard, L., Frost, D. J., McCammon, C. A., Dolejš, D., & Connolly, J. A. (2023). Experimental constraints on the ferric Fe content and oxygen fugacity in subducted serpentinites. *Journal of Petrology*, *64*(10), egad069. https://doi.org/10.1093/petrology/egad069

Egli, R. (2013). VARIFORC: An optimized protocol for calculating non-regular first-order reversal curve (FORC) diagrams. *Global and Planetary Change*, *110*, 302–320. https://doi.org/10.1016/j.gloplacha.2013.08.003

Epstein, G. S., Condit, C. B., Stoner, R. K., Holt, A. F., & Guevara, V. E. (2024). Evolving subduction zone thermal structure drives extensive forearc mantle wedge hydration. *AGU Advances*, *5*(4), e2023AV001121. https://doi.org/10.1029/2023av001121

Evans, K. A., & Frost, B. R. (2021). Deserpentinization in subduction zones as a source of oxidation in arcs: A reality check. *Journal of Petrology*, *62*(3), 1–32. https://doi.org/10.1093/petrology/egab016

Fabian, K., McEnroe, S. A., Robinson, P., & Shcherbakov, V. P. (2008). Exchange bias identifies lamellar magnetism as the origin of the natural remanent magnetization in titanohematite with ilmenite exsolution from Modum, Norway. *Earth and Planetary Science Letters*, *268*(3–4), 339–353. https://doi.org/10.1016/j.epsl.2008.01.034

Farahat, E. (2008). Chrome-spinels in serpentinites and talc carbonates of the El Ideid-El Sodmein District, central Eastern Desert, Egypt: Their metamorphism and petrogenetic implications. *Geochemistry*, *68*(2), 193–205. https://doi.org/10.1016/j.chemer.2006.01.003

Ferré, E. C., Kupenko, I., Martín-Hernández, F., Ravat, D., & Sanchez-Valle, C. (2020). Magnetic sources in the Earth's mantle. *Nature Reviews Earth & Environment*, *2*(1), 59–69. https://doi.org/10.1038/s43017-020-00107-x

Fish, B., Nichols, C. I. O., & Li, Y. (2025). Santa Catalina serpentinite magnetite EDS maps. *Zenodo*. https://doi.org/10.5281/zenodo.17061897

Gardonio, B., Marsan, D., Bodin, T., Socquet, A., Durand, S., Radiguet, M., et al. (2024). Change of deep subduction seismicity after a large megathrust earthquake. *Nature Communications*, *15*(1), 60. https://doi.org/10.1038/s41467-023-43935-3

Grove, M., & Bebout, G. E. (1995). Cretaceous tectonic evolution of coastal southern California: Insights from the Catalina Schist. *Tectonics*, *14*(6), 1290–1308. https://doi.org/10.1029/95TC01931

Grove, M., Bebout, G. E., Jacobson, C. E., Barth, A. P., Kimbrough, D. L., King, R. L., et al. (2008). The Catalina Schist: Evidence for middle Cretaceous subduction erosion of Southwestern North America. *Special Papers - Geological Society of America*, *436*, 335–361. https://doi.org/10.1130/2008.2436(15)

Haggerty, S. E. (1991). Oxide mineralogy of the upper mantle. *Reviews in Mineralogy and Geochemistry*, *25*(1), 355–416.

Haggerty, S. E. (1995). Upper mantle mineralogy. *Journal of Geodynamics*, *20*(4), 331–364. https://doi.org/10.1016/0264-3707(95)00016-3

Han, D., Nichols, C. I. O., McCarthy, W., & Li, Y. (2025). Santa Catalina serpentinite AMS stereonets. *Zenodo*. https://doi.org/10.5281/zenodo.17055490

Harrison, R. J., & Feinberg, J. M. (2008). FORCinel: An improved algorithm for calculating first-order reversal curve distributions using locally weighted regression smoothing. *Geochemistry, Geophysics, Geosystems*, *9*(5), Q05016. https://doi.org/10.1029/2008GC001987

Harrison, R. J., & Lascu, I. (2014). FORCulator: A micromagnetic tool for simulating first-order reversal curve diagrams. *Geochemistry, Geophysics, Geosystems*, *15*(12), 4671–4691. https://doi.org/10.1002/2014GC005582

Harrison, R. J., Muraszko, J., Heslop, D., Lascu, I., Muxworthy, A. R., & Roberts, A. P. (2018). An improved Algorithm for unmixing first-order reversal curve diagrams using principal component analysis. *Geochemistry, Geophysics, Geosystems*, *19*(5), 1595–1610. https://doi.org/10.1029/2018gc007511

Harrison, R. J., Zhao, X., Hu, P., Sato, T., Heslop, D., Muxworthy, A. R., et al. (2019). Simulation of remanent, transient, and induced FORC diagrams for interacting particles with uniaxial, cubic, and hexagonal Anisotropy. *Journal of Geophysical Research: Solid Earth*, *124*(12), 12404–12429. https://doi.org/10.1029/2019jb018050

Harvey, K. M., Penniston-Dorland, S. C., Kohn, M. J., & Piccoli, P. M. (2021). Assessing P-T variability in mélange blocks from the Catalina Schist: Is there differential movement at the subduction interface? *Journal of Metamorphic Geology*, *39*(3), 271–295. https://doi.org/10.1111/jmg.12571

Harvey, K. M., Walker, S., Starr, P. G., Penniston-Dorland, S. C., Kohn, M. J., & Baxter, E. F. (2021). A mélange of subduction ages: Constraints on the timescale of shear Zone development and underplating at the subduction interface, catalina schist (CA, USA). *Geochemistry, Geophysics, Geosystems*, *22*(9), e2021GC009790. https://doi.org/10.1029/2021GC009790

Hirose, F., Miyaoka, K., Hayashimoto, N., Yamazaki, T., & Nakamura, M. (2011). Outline of the 2011 off the Pacific coast of Tohoku Earthquake (M w 9.0) —Seismicity: Foreshocks, mainshock, aftershocks, and induced activity—. *Earth Planets and Space*, *63*(7), 513–518. https://doi.org/10.5047/eps.2011.05.019

Hodel, F., Macouin, M., Trindade, R. I., Araujo, J. F., Respaud, M., Meunier, J. F., et al. (2020). Magnetic properties of ferritchromite and Cr-Magnetite and monitoring of Cr-Spinels alteration in ultramafic and mafic rocks. *Geochemistry, Geophysics, Geosystems*, *21*(11), e2020GC009227. https://doi.org/10.1029/2020GC009227

Holland, T. J. B., & Powell, R. (2011). An improved and extended internally consistent thermodynamic dataset for phases of petrological interest, involving a new equation of state for solids: Thermodynamic dataset for phases of Petrological interest. *Journal of Metamorphic Geology*, *29*(3), 333–383. https://doi.org/10.1111/j.1525-1314.2010.00923.x

Koopmans, L., McCarthy, W., & Magee, C. (2022). Dyke Architecture, mineral layering, and magmatic convection; new perspectives from the younger giant dyke complex, S Greenland. *Geochemistry, Geophysics, Geosystems*, *23*(3), e2021GC010260. https://doi.org/10.1029/2021gc010260

Lascu, I., Einsle, J. F., Ball, M. R., & Harrison, R. J. (2018). The Vortex State in geologic materials: A micromagnetic perspective. *Journal of Geophysical Research: Solid Earth*, *123*(9), 7285–7304. https://doi.org/10.1029/2018JB015909

Latimer, B., McCarthy, W., Mattsson, T., & Reavy, J. (2024). Enclaves as mushy magma strain archives: New perspectives on composite magmatic fabrics in plutons. *Geosphere*, *20*(5), 1390–1410. https://doi.org/10.1130/ges02786.1

Lay, T., Kanamori, H., Ammon, C. J., Nettles, M., Ward, S. N., Aster, R. C., et al. (2005). The Great Sumatra-Andaman Earthquake of 26 December 2004. *Science*, *308*(5725), 1127–1133. https://doi.org/10.1126/science.1112250

Lee, C., & Kim, Y. (2021). Role of warm subduction in the seismological properties of the forearc mantle: An example from southwest Japan. *Science Advances*, *7*(28), eabf8934. https://doi.org/10.1126/sciadv.abf8934

Li, Y. (2025). Santa Catalina Serpentinisation (Jupyter notebooks). *Zenodo*. https://doi.org/10.5281/zenodo.15142789

Li, Y., Harrison, R. J., & Nichols, C. I. O. (2025). Santa Catalina AGM (Magnetic Data) processing project. *Zenodo*. https://doi.org/10.5281/zenodo.15098465

Li, Y., & Nichols, C. I. O. (2024a). Santa Catalina serpentinite reflected light scans. *Zenodo*. https://doi.org/10.5281/zenodo.13329989

Li, Y., & Nichols, C. I. O. (2024b). Santa Catalina EPMA spot analysis locations. *Zenodo*. https://doi.org/10.5281/zenodo.13685581

Li, Y., Nichols, C., & Lindquist, P. (2024). Santa Catalina vein geochemical profiles. https://doi.org/10.5281/zenodo.13685560

Li, Y., Palin, R. M. P., & Nichols, C. I. O. (2024). Santa Catalina serpentinite petrography. *Zenodo*. https://doi.org/10.5281/zenodo.13824006

Lindquist, P., & Li, Y. (2024). Santa Catalina serpentinite vein EDS maps. *Zenodo*. https://doi.org/10.5281/zenodo.13351361

Manea, M., & Manea, V. C. (2011). Curie point depth estimates and correlation with subduction in Mexico. *Pure and Applied Geophysics*, *168*(8–9), 1489–1499. https://doi.org/10.1007/s00024-010-0238-2

Mattsson, T., Petri, B., Almqvist, B., McCarthy, W., Burchardt, S., Palma, J. O., et al. (2021). Decrypting magnetic fabrics (AMS, AARM, AIRM) through the analysis of mineral shape fabrics and distribution Anisotropy. *Journal of Geophysical Research: Solid Earth*, *126*(6), e2021JB021895. https://doi.org/10.1029/2021jb021895

Maus, S., & Haak, V. (2002). Is the Long Wavelength Crustal Magnetic Field Dominated by Induced or by Remanent Magnetisation. Retrieved from https://api.semanticscholar.org/CorpusID:5656709

Mertzman, S. (2000). K-Ar results from the southern Oregon-northern California Cascade Range. *Oregon Geology*, *62*(4), 99–122.

Okubo, Y., Graf, R. J., Hansen, R. O., Ogawa, K., & Tsu, H. (1985). Curie point depths of the Island of Kyushu and surrounding areas, Japan. *Geophysics*, *50*(3), 481–494. https://doi.org/10.1190/1.1441926

Oliver, N. H., & Bons, P. D. (2001). Mechanisms of fluid flow and fluid-rock interaction in fossil metamorphic hydrothermal systems inferred from vein-wall rock patterns, geometry and microstructure. *Geofluids*, *1*(2), 137–162. https://doi.org/10.1046/j.1468-8123.2001.00013.x

Penniston-Dorland, S. C., Kohn, M. J., & Piccoli, P. M. (2018). A mélange of subduction temperatures: Evidence from Zr-in-rutile thermometry for strengthening of the subduction interface. *Earth and Planetary Science Letters*, *482*, 525–535. https://doi.org/10.1016/j.epsl.2017.11.005

Platt, J. P. (1975). Metamorphic and deformational processes in the Franciscan Complex, California: Some insights from the Catalina Schist terrane. *Bulletin of the Geological Society of America*, *86*(10), 1337–1347. https://doi.org/10.1130/0016-7606(1975)86<1337:MADPIT>2.0.CO;2

Platt, J. P. (1976). *The petrology, structure, and geologic history of the Catalina Schist terrain, Southern California*. University of California Press.

Platt, J. P., Grove, M., Kimbrough, D. L., & Jacobson, C. E. (2020). Structure, metamorphism, and geodynamic significance of the Catalina Schist terrane. In *From the islands to the mountains: A 2020 view of geologic excursions in southern california* (pp. 165–195). Geological Society of America. https://doi.org/10.1130/2020.0059(05)

Platt, J. P., & Schmidt, W. L. (2024). Is the inverted field gradient in the catalina schist terrane primary or constructional? *Tectonics*, *43*(2), e2023TC008021. https://doi.org/10.1029/2023TC008021

Ravat, D., Pignatelli, A., Nicolosi, I., & Chiappini, M. (2007). A study of spectral methods of estimating the depth to the bottom of magnetic sources from near-surface magnetic anomaly data. *Geophysical Journal International*, *169*(2), 421–434. https://doi.org/10.1111/j.1365-246X.2007.03305.x

Reynard, B. (2013). Serpentine in active subduction zones. *Lithos*, *178*, 171–185. https://doi.org/10.1016/j.lithos.2012.10.012

Roberts, A. P., Heslop, D., Zhao, X., & Pike, C. R. (2014). Understanding fine magnetic particle systems through use of first-order reversal curve diagrams. *Reviews of Geophysics* (Vol. 52, pp. 557–602). Blackwell Publishing Ltd. https://doi.org/10.1002/2014RG000462

Roberts, A. P., Tauxe, L., Heslop, D., Zhao, X., & Jiang, Z. (2018). A critical appraisal of the "Day" diagram. *Journal of Geophysical Research: Solid Earth*, *123*(4), 2618–2644. https://doi.org/10.1002/2017jb015247

Saad, A. H. (1969). Magnetic properties of ultramafic rocks from Red Mountain, California. *Geophysics*, *34*(6), 974–987. https://doi.org/10.1190/1.1440067

Sagnotti, L. (2020). Magnetic anisotropy. In *Encyclopedia of Solid Earth Geophysics* (pp. 1–13). Springer International Publishing. https://doi.org/10.1007/978-3-030-10475-7_113-1

Schult, A. (1970). Effect of pressure on the Curie temperature of titanomagnetites [(1 x). Fe3O4 x. TiFe2O4]. *Earth and Planetary Science Letters*, *10*(1), 81–86. https://doi.org/10.1016/0012-821x(70)90067-1

Siebert, L., Cottrell, E., Venzke, E., & Andrews, B. (2015). *Earth's Volcanoes and Their Eruptions: An Overview*. (pp. 239–255). Elsevier. https://doi.org/10.1016/B978-0-12-385938-9.00012-2

Sorensen, S. S. (1988). Petrology of amphibolite-facies mafic and ultramafic rocks from the Catalina Schist, southern California: Metasomatism and migmatization in a subduction zone metamorphic setting. *Journal of Metamorphic Geology*, *6*(4), 405–435. https://doi.org/10.1111/j.1525-1314.1988.tb00431.x

Sorensen, S. S., & Barton, M. D. (1987). Metasomatism and partial melting in a subduction complex Catalina Schist, southern California. *Geology*, *15*(2), 115. https://doi.org/10.1130/0091-7613(1987)15⟨115:mapmia⟩2.0.co;2

Sridhar, S., Bryson, J. F., King, A. J., & Harrison, R. J. (2021). Constraints on the ice composition of carbonaceous chondrites from their magnetic mineralogy. *Earth and Planetary Science Letters*, *576*, 117243. https://doi.org/10.1016/j.epsl.2021.117243

Syracuse, E. M., van Keken, P. E., Abers, G. A., Suetsugu, D., Bina, C., Inoue, T., & Jellinek, M. (2010). The global range of subduction zone thermal models. *Physics of the Earth and Planetary Interiors*, *183*(1–2), 73–90. https://doi.org/10.1016/j.pepi.2010.02.004

Tanaka, A., Okubo, Y., & Matsubayashi, O. (1999). Curie point depth based on spectrum analysis of the magnetic anomaly data in East and Southeast Asia. *Tectonophysics*, *306*(3–4), 461–470. https://doi.org/10.1016/s0040-1951(99)00072-4

Tarling, D., & Hrouda, F. (1993). *Magnetic anisotropy of rocks* (1st ed.), (Vol. 1). Springer. Retrieved from https://link.springer.com/book/9780412498800

Teknik, V., Artemieva, I. M., & Thybo, H. (2024). Limited arc magmatism and seismicity due to extensive mantle wedge serpentinization in the Makran subduction zone. *Earth and Planetary Science Letters*, *645*(118950), 118950. https://doi.org/10.1016/j.epsl.2024.118950

Thébault, E. (2021). Magnetic anomalies: Interpretation. *Encyclopedia of Earth Sciences Series*, 935–943. https://doi.org/10.1007/978-3-030-58631-7_118

Tyler, D. J., & Danielson, J. J. (2018). Topobathymetric Model for the Southern Coast of California and the channel Islands, 1930 to 2014. *U.S. Geological Survey*. https://doi.org/10.5066/P9UZIYI8

van Keken, P. E., & Wilson, C. R. (2023). An introductory review of the thermal structure of subduction zones: I—Motivation and selected examples. *Progress in Earth and Planetary Science*. In (Vol. 10) Springer Science and Business Media Deutschland GmbH. https://doi.org/10.1186/s40645-023-00573-z. 42.

Waterton, P., Pearson, D. G., Mertzman, S. A., Mertzman, K. R., & Kjarsgaard, B. A. (2020). A fractional crystallization link between Komatiites, basalts, and dunites of the palaeoproterozoic winnipegosis komatiite Belt, Manitoba, Canada. *Journal of Petrology*, *61*(5), egaa052. https://doi.org/10.1093/petrology/egaa052

Whitney, D. L., & Evans, B. W. (2010). Abbreviations for names of rock-forming minerals. *American Mineralogist*, *95*(1), 185–187. https://doi.org/10.2138/am.2010.3371

Xia, S., Sun, J., & Huang, H. (2015). Degree of serpentinization in the forearc mantle wedge of Kyushu subduction zone: Quantitative evaluations from seismic velocity. *Marine Geophysical Researches*, *36*(2–3), 101–112. https://doi.org/10.1007/s11001-014-9239-3

Xu, J., Jiang, Z., Zhang, X., Li, S., Li, X., Chen, L., et al. (2025). Effects of subduction fluids and fractional crystallization on the magnetic minerals formation in the back-arc Basin. *Geophysical Research Letters*, *52*(10), e2025GL115006. https://doi.org/10.1029/2025gl115006

## References From the Supporting Information

Oufi, O., Cannat, M., & Horen, H. (2002). Magnetic properties of variably serpentinized abyssal peridotites. *Journal of Geophysical Research*, *107*(B5), EPM3-1–19. https://doi.org/10.1029/2001jb000549

Pastore, Z., McEnroe, S. A., ter Maat, G. W., Oda, H., Church, N. S., & Fumagalli, P. (2018). Mapping magnetic sources at the millimeter to micrometer scale in dunite and serpentinite by high-resolution magnetic microscopy. *Lithos*, *323*, 174–190. https://doi.org/10.1016/j.lithos.2018.09.018

ter Maat, G. W., McEnroe, S. A., Church, N. S., & Larsen, R. B. (2019). Magnetic mineralogy and petrophysical properties of ultramafic rocks: Consequences for crustal magnetism. *Geochemistry, Geophysics, Geosystems*, *20*(4), 1794–1817. https://doi.org/10.1029/2018GC008132